The separating flow in a plane asymmetric diffuser with 8.5° opening angle: mean flow and turbulence statistics, temporal behaviour and flow structures

OLLE TÖRNBLOM†‡, BJÖRN LINDGREN¶ AND ARNE V. JOHANSSON

KTH Mechanics, SE-100 44 Stockholm, Sweden

The flow in a plane asymmetric diffuser with an opening angle of 8.5° has been studied experimentally using time-resolving stereoscopic particle image velocimetry. The inlet condition is fully developed turbulent channel flow at a Reynolds number based on the inlet channel height and bulk velocity of $Re = 38\,000$. All mean velocity and Reynolds stress components have been measured. A separated region is found on the inclined wall with a mean separation point at 7.4 and a mean reattachment point at 30.5 inlet channel heights downstream the diffuser inlet (the inclined wall ends 24.8 channel heights downstream the inlet). Instantaneous flow reversal never occurs upstream of five inlet channel heights but may occur far downstream the point of reattachment. A strong shear layer in which high rates of turbulence production are found is located in a region outside the separation. The static wall pressure through the diffuser is presented and used in an analysis of the balance between pressure forces and momentum change. It is demonstrated that production of turbulence causes a major part of the losses of mean flow kinetic energy. The character of the large turbulence structures is investigated by means of time-resolved sequences of velocity fields and spatial auto-correlation functions. Pronounced inclined structures are observed in the spanwise velocity and it is suggested that these are due to the legs of hairpin-like vortices.

1. Introduction

Wall-bounded fluid flow at large Reynolds numbers may, due to rather small changes in the wall direction or pressure gradient, detach from the wall and form a region of reversed flow next to the wall. This phenomenon is referred to as flow separation. The properties of a flow that separates and a flow in a similar geometry that stays attached can be completely different and separating flow is often associated with decreasing performance of a device due to increased losses of mechanical energy.

Diffusers, i.e. ducts with a cross-sectional area that is increasing in the streamwise direction, are used in many engineering applications. A common purpose of diffusers is to reduce the velocity of a subsonic flow and hence regain pressure. If the flow

† Email address for correspondence: olle@mech.kth.se
‡ Present address: Studsvik Nuclear AB, SE-611 82, Nyköping, Sweden
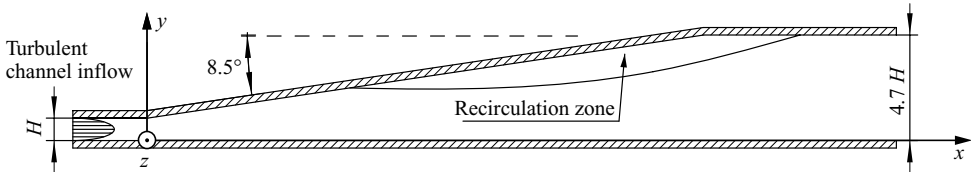¶ Present address: Scania CV AB, SE-151 87, Södertälje, Sweden

FIGURE 1. The plane asymmetric diffuser of the present investigation. A part of the inlet channel is seen on the left and part of the outlet channel is seen on the right. The view is from the top as referred to in figure 2.

separates in the diffuser, the recovered pressure will, in most cases, be smaller than if the flow would have stayed attached. A separation can also introduce undesired low-frequency fluctuations in the flow.

The plane asymmetric diffuser flow, originally introduced by Shinnosuke Obi, is a suitable case for fundamental studies of internal flows where the separation occurs on a smooth wall (see figure 1). The inlet conditions are well defined and can, in a consistent manner, be replicated in computations. The asymmetric shape favours separation on the side with the diverging wall and in this way avoids the problem with an alternating asymmetric separation that one may have in a symmetric geometry. The mean flow is approximately two-dimensional, which facilitates the implementation of the geometry in codes for large-eddy simulation (LES) or direct numerical simulation (DNS) and it also enables averaging in the spanwise direction when computing turbulence statistics. The two-dimensionality will, of course, also simplify testing of turbulence models. The geometry is fairly simple, which makes it easy to achieve good computational grids. It has, for example, been shown by Brüger et al. (2004) that a numerical conformal mapping for an orthogonal curvilinear grid can be derived for the diffuser.

The first investigation of the plane asymmetric diffuser (known to the present authors) is that by Obi, Aoki & Masuda (1993a). In that study the in-plane velocities and Reynolds stresses in a 10° diffuser were measured using a single component laser Doppler velocimeter (LDV) and compared to computations with two different turbulence models.

Obi et al. (1993b) continued to study the same flow experimentally, now affecting the flow with a periodic perturbation. The perturbation was generated by blowing and suction through a slit in the spanwise direction. They investigated the influence of the perturbation frequency on the size of the separation bubble and found that the largest reduction of the separation size occurred at a non-dimensional frequency, based on the inlet channel height and the inlet channel centreline velocity, around $St = 0.03$.

Obi, Ishibashi & Masuda (1997) further investigated the effect of the perturbation on the production of the turbulent Reynolds shear stress, separating the contributions from the perturbation and the mean flow. They found that at the optimum frequency, regarding separation reduction, both the production of Reynolds shear stress and the interaction between the mean flow and the perturbation were enhanced. Obi, Nikaido & Masuda (1999) investigated the Reynolds number dependence of the 10° diffuser flow, and found that the separation, measured in the centre region of the diffuser, diminished with decreasing Reynolds number. However, it is pointed out that the observed dependency is a bit uncertain due to a deficiency in the two-dimensionality of the flow present at the lower Reynolds numbers.

Another experimental investigation of the $10°$ diffuser is that by Buice & Eaton (1997, 2000). The primary measurement method used was pulsed hot-wires, and thermal tufts were used to find the separation and reattachment points. The locations of these points were determined at $x/H = 6.5$–7.0 and 29, respectively. Energy spectra measured by Buice & Eaton in the outlet channel showed high energy levels at low frequencies but no isolated peaks that could indicate existence of a dominant frequency of the separation.

The plane asymmetric diffuser has also been subject to a few computational studies of fundamental character. An extensive numerical study of the $10°$ case was made by Kaltenbach *et al.* (1999), who performed an LES at a Reynolds number of 1000 based on the inlet channel height and the inlet friction velocity. The results of Kaltenbach *et al.* showed good agreement for velocity profiles with the experimental data of both Obi *et al.* and Buice & Eaton. The point of separation agreed well with that found by Buice & Eaton, but the reattachment point was found farther downstream in the LES. A possible reason for this can be the relatively small spanwise width of the computational domain ($4H$), which may artificially enhance spanwise coherence of large-scale structures. Kaltenbach *et al.* (1999) found that the subgrid scale model plays an essential role to calculate the flow correctly, since subgrid stresses give a major contribution to the wall-shear stress.

LES was also the tool used in the study by Herbst (2006), where primarily the Reynolds number dependency of the $8.5°$ diffuser flow was investigated. Simulations performed at $Re_H = U_b H/\nu = 9000$, $18\,000$ and $40\,000$ revealed a trend towards an increasing size of the separation with increasing Reynolds number. However, the Reynolds number dependence appeared to be diminishing with increasing Reynolds number so that one may expect a constant separation size for Reynolds numbers over a certain limit. Much of the physics behind this, slightly counter-intuitive, phenomenon remains to be clarified. Herbst also shows that the tendency towards separation on the curved upper corner due to flow curvature follows an opposite trend, at the lowest Reynolds number a small separation is seen but it disappears with increasing Reynolds number.

Wu *et al.* (2006) used LES to investigate an internal layer that forms along the plane wall of the $10°$ diffuser. The internal layer was also observed in the $8.5°$ diffuser by Herbst, who reported that this layer was more pronounced at higher Reynolds numbers.

Several turbulence model investigations have used the plane asymmetric diffuser as a reference case. In an Ercoftac workshop (Hellsten & Rautaheimo 1999), the results from computations of the $10°$ case using a great number of turbulence models are summarized. Gullman-Strand (2004) made an extensive investigation of the performance of explicit algebraic Reynolds stress and scalar flux models in both the $8.5°$ and the $10°$ diffuser.

Previous experimental investigations of the plane asymmetric diffuser flow have mainly been concerned with single point statistics. Buice & Eaton measured spanwise two-point correlations of the streamwise velocity fluctuations, but apart from this, knowledge of the structural character of this flow has been limited. The LES studies by both Kaltenbach *et al.* (1999) and Herbst (2006) presented visualizations of instantaneous flow reversal in the plane asymmetric diffuser, showing that the separation process is highly irregular and unsteady. Herbst also shows that the elongated near-wall structures of the streamwise velocity component (streaks) are broken up in the separated region.

In general, the literature on the structural character of turbulent flows separating from smooth walls is quite scarce. However, a recent investigation is done by Song & Eaton (2004), who studied the flow structures of a separating, reattaching and recovering boundary layer over a smooth ramp, using instantaneous particle image velocimetry (PIV) realizations of the flow and auto-correlations of the in-plane velocities. They found evidence for the existence of roller vortices, generated by the Kelvin–Helmholtz instability of the separated shear layer. They also concluded that around, and after, reattachment these roller vortices are often distorted by the mean flow gradients (both $\partial U/\partial y$ and $\partial U/\partial x$ contribute) forming structures similar to the hairpin vortices in a flat-plate boundary layer. Although undergoing the same processes (separation from a smooth wall, reattachment and recovery) the flow studied by Song & Eaton differs from the present in at least two important aspects: (*i*) the present flow is confined between two walls without a free-stream and (*ii*) the separated region in the present flow is substantially larger in relation to the upstream boundary-layer thickness.

The aim of the present study is to give a comprehensive description of the flow in the 8.5° diffuser and its nearby surroundings by studying statistical single-point flow properties, integrated quantities describing conservation of mass, momentum and energy as well as the structural character of the turbulence. The separated region is given special attention in that we look at measures such as the backflow coefficient and the mean dividing streamline.

2. Experimental set-up and measurement methods

The reason for choosing a smaller diffuser opening angle, in comparison to previous investigations, was to reduce the size of the separated region and thereby reduce the unsteadiness of the separation and reattachment points and in combination with a high-aspect ratio of the diffuser, achieve a mean flow less prone to be three-dimensional. It is also likely that predicting a correct separation in a geometry with a smaller opening angle is a more demanding challenge for turbulence models. Support for this presumption was found in Gullman-Strand *et al.* (2004), where a model giving a reasonably accurate size of the separation bubble in the 10° case predicted too small a bubble when the angle was 8.5°.

Here follows a condensed description of the experimental set-up and the measurement procedures; for a more detailed description the reader is referred to Törnblom (2006).

2.1. *Description of the wind-tunnel*

The experiments were performed in a closed loop wind-tunnel built specifically for this investigation. The wind-tunnel can be seen in figure 2. It consists of a blowing centrifugal fan followed by a section transforming the rectangular cross-section shape of the blower outlet to another one with much higher aspect ratio. In this section, splitter plates and screens ensure an even distribution of the fluid over the cross-section area. The transformer is followed by a straight duct (settling chamber) which contains two screens at its upstream end to further even out mean flow variations. At the downstream end of the settling chamber is a two-dimensional contraction leading the flow into a 3200 mm long channel with a cross-section area (width to height) of 1525×30 mm². The channel height, $H = 30$ mm, is a length scale frequently used for normalization in the present article. The length to height ratio of the channel is larger than 100, ensuring fully developed channel flow at the downstream end (see e.g. Comte-Bellot 1965). Johansson & Alfredsson (1981) measured the mean velocity,
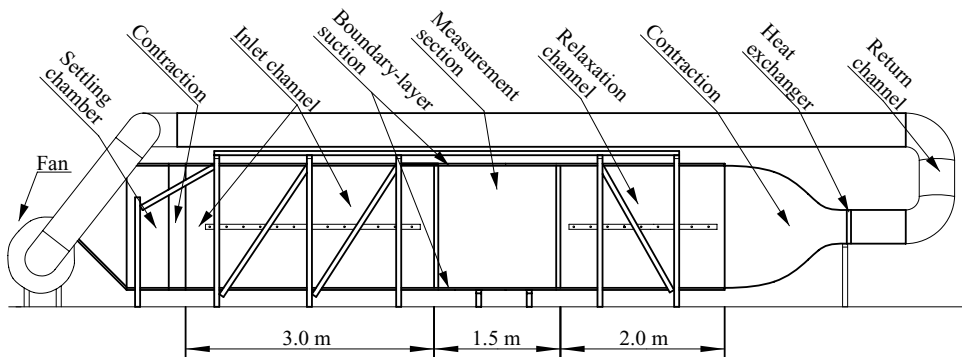
FIGURE 2. The wind-tunnel used in the experiments. The flow is circulating counter clockwise.

root mean square (r.m.s.), skewness and flatness of the streamwise velocity on the centreline of a channel flow at various downstream positions. They found even the higher moments to attain values close to the asymptotic ones after about 60 channel heights, which further supports the assumption of a fully developed flow at the end of the inlet channel, thereby ensuring well-defined inlet boundary conditions for the diffuser flow.

At the endwalls (limiting the spanwise width of the channel) the boundary layers are removed by means of suction through 100 mm long perforated regions located at the downstream end of the inlet channel. This is done to prevent the endwall boundary layers from separating in the adverse pressure gradient of the diffuser. The boundary layer removal is described in more detail by Törnblom (2006). The centreline velocity of the incoming channel flow was measured, using a Pitot-tube at six different spanwise positions and found to vary by less than $\pm 0.9\%$ over the full spanwise width.

The diffuser has an inclined wall with an angle of $8.5°$ (see figure 1) on one side and a straight wall on the other. Both the convex upstream and the concave downstream corners of the inclined wall are rounded with a radius of 300 mm ($10H$). The straight wall and the endwalls are made of Plexiglas so as to allow the use of optical measurement techniques. The straight wall is equipped with pressure taps, at an interval of 25 mm, in a row along the centreline. The inclined wall has a sparser row of pressure taps along its centreline. After the diffuser follows an outlet channel which is 141 mm high ($4.7H$) and 2500 mm long. The purpose of this channel is to avoid upstream influence on the flow from devices located farther downstream. The outlet channel is followed by a three-dimensional transformer and a heat exchanger which keeps the temperature steady within $\pm 0.5\,°C$. After the heat exchanger a pipe, 400 mm diameter, leads the flow back to the fan. At the end of the pipe, the seeding particles (see §2.3) are injected into the flow.

2.2. *Pressure measurements*

Pressures were measured using a Furness Control FCO 510 differential pressure transducer with an accuracy of 0.25 % of full scale (2000 Pa). The holes through which the static pressure is measured are drilled directly in the plexiglas of the plane diffuser wall and have a diameter of 0.4 mm.

The skin-friction of the inlet channel flow was measured at $x/H = -3.3$ using a Preston tube and the pressure transducer described above. During the PIV measurements, the Preston tube was used to continuously monitor the friction
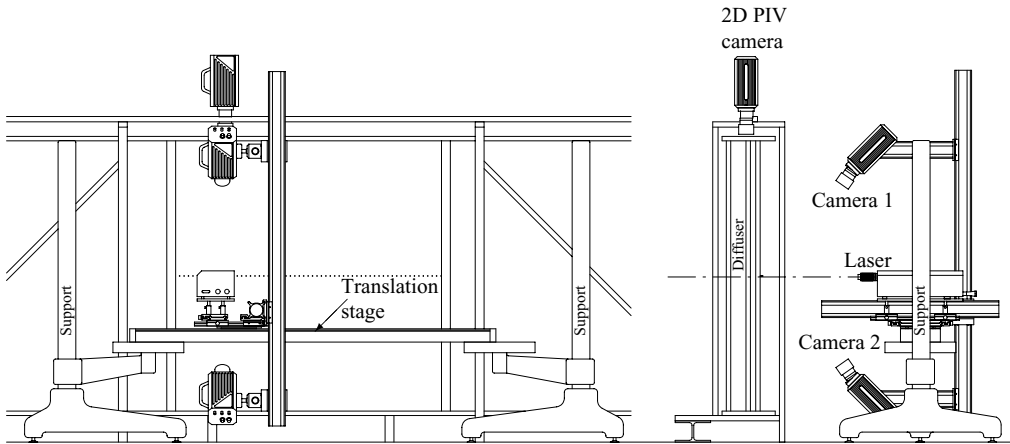
FIGURE 3. A sketch showing two views of the PIV set-up. The y- and x-directions (cf. figure 1) are perpendicular to the paper plane in the left and right views, respectively.

velocity, u_τ, and the fan speed was regulated in order to keep this quantity constant within $\pm 0.3\%$. The air density and viscosity used in the calculation of u_τ were calculated based on continuous measurements of the atmospheric pressure and the air temperature in the wind-tunnel.

2.3. *PIV measurements*

Stereoscopic PIV was used to measure the mean velocities and turbulence statistics in three spatial directions. The set-up for the measurements is shown in figure 3. The laser light sheet is horizontal, and in the diffuser mid-plane the two cameras image the measurement plane at an angle of approximately 30 degrees with respect to its normal direction. The laser head and the cameras are mounted on a translation stage which allows the set-up to be moved, for measurements at different streamwise stations, without changing the camera–lightsheet geometry.

The PIV system consists of a New Wave Pegasus diode pumped Nd:YLF laser with dual heads, two Photron Ultima APX-RS cameras with $1\,024 \times 1\,024$ pixels and acquisition hardware and software from LaVision. The maximum frame rate of the cameras at full resolution is 3 kHz, and with reduced resolution the cameras can run at rates up to 250 kHz. Nikon $f = 50$ mm lenses are used on the cameras at a large aperture together with a Scheimpflug arrangement which enables oblique focusing on the light sheet. The average light sheet thickness was estimated to be 1.5 mm by analysing the correlation peak widths of cross-correlations between particle images from different cameras, taken at the same instant (Wieneke 2005).

The laser has its maximum energy output per pulse when each head is running at a rate of 1 kHz. Therefore, the PIV system was ran at this rate when sampling for statistics, but only every tenth image pair was kept in order to have statistically independent samples. The cameras can collect 3072 image pairs before it is necessary to transfer the images from their memories to a hard-drive. The data sets from which the statistics have been computed consist therefore of data collected at a rate of 100 Hz at 10 different occasions. The total number of samples was 3080 and the time required to collect such a set was approximately one hour. In order to cover the whole flow field, 18 slightly overlapping sets were collected at different streamwise positions in the diffuser. The time between the laser pulses was optimized for each set and

varied with the downstream position. The presented two-component measurements were collected similarly but are based on 4920 samples.

A first calibration of the stereoscopic set-up was performed in the wider outlet channel of the diffuser using a calibration plate mounted on a translation stage. Then, at each measurement position a correction of the original calibration was made using particle images and the self-calibration method described by Wieneke (2005). This procedure gave a matching of the images from the two cameras which deviated less than 0.1 pixels.

The recorded images were preprocessed by subtracting a sliding average of five, in the time sequence, consecutive images. The velocity vector fields were calculated using a multi-pass cross-correlation method similar to that of Scarano & Riethmuller (2000). The physical size of the 32×32 pixel interrogation areas is $4.7 \times 4.7\,\text{mm}^2$, or $0.16 \times 0.16H^2$ in non-dimensional units and the interrogation area overlap is 50 %.

High-resolution measurements were performed in a region near the separation point, using two-component PIV. The camera was then positioned over the measurement section, as indicated in figure 3, and the interrogation area width was $0.94 \times 0.94\,\text{mm}^2$ $(0.031 \times 0.031H^2)$.

The air was seeded with particles from a smoke generator using a mixture of glycerol and water. The smoke was inserted just upstream of the fan and was sufficiently spread out in the measurement section due to the mixing in the fan and the inlet channel. An estimate of the particle size, based on recorded particle images and using relations for the Airy pattern given by Raffel, Willert & Kompenhans (1997), showed that the particles are approximately $3\,\mu\text{m}$ in diameter. Assuming Stokes drag, particles with this diameter will have a response time of the same order as the Kolmogorov time scale of the inlet channel flow.

2.4. *Measurement quality*

A typical value for the measurement error in digital PIV with 32×32 pixel interrogation areas is 0.05 to 0.1 pixel (Westerweel 1997), given that the measurement conditions fulfil a number of criteria. In the forthcoming, these conditions and criteria are discussed in conjunction with the present experiment.

It was ensured in all measurements that the particle concentration was sufficient, i.e. $\geqslant 10$ particles in each interrogation area according to Keane & Adrian (1992). Bias due to out-of-plane loss of particle pairs is small. An estimate based on the maximum turbulent velocity, $\sqrt{\overline{ww}}$, showed that if the distribution of w is assumed to be Gaussian, 99 % of samples will fulfil the 'one quarter rule' given by Keane & Adrian (1990). Problems with in-plane loss of pairs are avoided in the cross-correlation algorithm used. Furthermore, the interrogation window deformation of the cross-correlation algorithm reduces the correlation noise due to velocity gradients (Scarano & Riethmuller 2000).

The degree of peak-locking in the measured data has been investigated and found to be very small. The particle image diameter is around 2 pixels, which should be near optimum with respect to minimizing peak-locking (Raffel *et al.* 1997) and the cross-correlation algorithm used is also contributing in this aspect (Scarano & Riethmuller 2000).

The present stereoscopic set-up will result in a decreased uncertainty of the measured in-plane components as compared with a similar non-stereoscopic set-up. The uncertainty of the out-of-plane component is approximately twice that of the in-plane components.

In the stereoscopic PIV measurements, the time between frames was 50–70 μs for the five most upstream profiles. Hence, assuming a measurement error of 0.1 pixel gives a maximum measurement uncertainty of $\pm 1.5\%$ of U_b. The rest of the stereoscopic data were acquired with a time between frames of 100 μs, giving an uncertainty of $\pm 0.75\%$ of U_b.

The statistical uncertainty of the presented mean velocities is proportional to the turbulent velocity magnitude and is with 95 % reliability smaller than $\pm 0.38\%$ of U_b for the U mean velocity and smaller than $\pm 0.26\%$ of U_b for V.

2.5. *Comparison between fine and coarse resolution measurements*

Fine resolution measurements, using two-component PIV, were performed in a region around the separation point. Figure 4 gives a comparison of the measurements with finer and coarser resolution. The agreement in the streamwise mean velocity (figure 4a) is very close and the mean velocities in the y-direction (figure 4c) collapse without any visible bias, although the profiles are somewhat uneven.

The measured velocity variances are slightly biased towards smaller values in the coarser data set. This is due to the spatial low-pass filtering which follows from the integration over the interrogation areas. Stereoscopic PIV will, in one direction, suffer more from spatial filtering as compared to two-dimensional PIV (see van Doorne 2004). This is because of the oblique viewing through a light sheet with a non-zero thickness. In the present stereoscopic set-up, the measurement volume is largest in the y-direction, in which the effective measurement volume length is approximately 5.6 mm, as compared to 4.7 and 1.5 mm in the x- and z-directions, respectively. The stronger spatial filtering in the y-direction can be seen in the comparison of the measurements of $\overline{vv}$ in figure 4(d), where a discrepancy of approximately 25 % is seen, while the measurements of $\overline{uu}$ shown in figure 4(b) only differ by around 15 %. The spatial filtering has a smaller impact on the fine resolution measurements where the length scale of the interrogation areas is 1/5 of that in the coarser measurements and the viewing direction is perpendicular to the light sheet.

The correlation $\overline{uv}$ (see figure 4e) does not display any bias, probably because it is governed mainly by the large-scale fluctuations.

The spatial filtering can be expected to have larger impact on the fluctuation levels measured close to walls and in the upstream part of the diffuser where a larger part of the turbulence energy spectrum resides in scales smaller than the measurement volume.

3. Mean flow and single-point turbulence statistics

We here focus on the mean velocity components and fluctuation intensities. Results are also presented for the turbulent kinetic energy and its production. Properties of both the streamfunction and backflow coefficient, which characterize the mean properties of the separated region, are presented. The static pressure coefficient along the straight wall is also shown as well as some integrated quantities which give insight into the mass, momentum and energy balance of the flow.

3.1. *Velocity components*

The results are presented in a right-handed coordinate system with x in the "streamwise" direction, y in the in-plane, transverse direction and z in the spanwise direction; see figures 1 and 2. The corresponding average velocities are denoted by U, V and W, respectively, and the lower-case versions of the same letters are used to denote fluctuations. In all figures, the spatial coordinates are normalized with the inlet
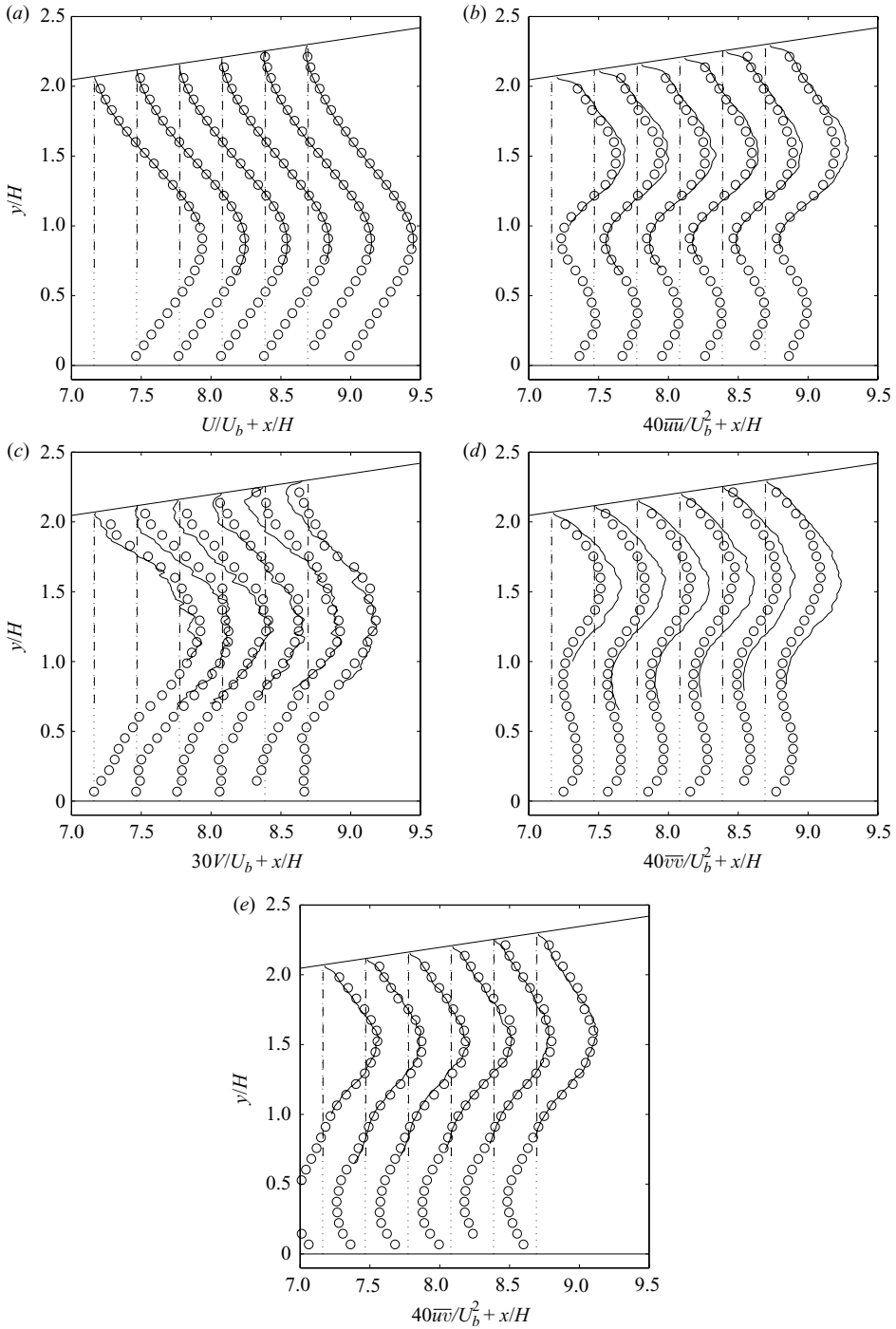
FIGURE 4. Fine resolution PIV measurements around the separation point (the solid lines) compared with the coarser data set (symbols).

channel height, $H = 30$ mm, and the velocities are normalized with the inlet channel bulk velocity, $U_b = 18.8$ m s^{-1}, defined as

$$U_b = \left(\frac{1}{H} \int_0^H U \mathrm{d}y \right)_{x=-2H}. \tag{3.1}$$

Due to lack of near-wall data from the inlet channel, U_b is approximated using the centreline velocity, U_{cl} at $x = -2H$, in the inlet channel and Dean's empirical relation

$$\frac{U_{cl}}{U_b} = 1.28 \left(\frac{U_b H}{2\nu} \right)^{-0.0116}. \tag{3.2}$$

Several figures show the development of different scalar flow quantities as a series of profiles taken along lines with constant x-coordinates. The profiles are scaled with a constant factor (cf. x-axis labels) in order to increase clarity and plotted so that their zero levels collapse with their x-coordinate. Measurement points near the walls have deliberately been removed in the figures showing the coarser data set of the complete diffuser. This was done because of the increased measurement uncertainty of these data points due to possible overlap of the relatively large interrogation areas and the wall. The removal was done ad hoc and the wall-normal position of the first points is varying.

The inlet length upstream the diffuser is chosen as 200 half-channel heights so as to ensure that any deviations from a fully developed channel flow are minimal. For comparisons between the present diffuser flow data and RANS or LES/DNS computations, one could therefore recommend to use DNS channel flow profiles as inlet conditions.

3.1.1. Streamwise mean and fluctuating velocities

The diffuser flow is characterized by a jet-like high-velocity region that follows the straight wall and low-velocity region along the inclined wall; see figures 5 and 4(*a*). In between these two regions is a layer of strong shear. From $x/H \approx 6$ and downstream the peaks of the U-velocity profiles stay at approximately the same distance from the straight wall, although the peaks are quite diffused in the most downstream profiles. A relatively high peak velocity is maintained over the region in x where the separation bubble height is increasing because the effective diffuser angle is nearly zero here due to displacement from the recirculation region. The small decrease in peak velocity which is yet seen in this region is mainly due to a spreading of the peak that most likely can be attributed to turbulent diffusion.

There are easily recognizable inflection points on the low-velocity side of the profiles but less pronounced inflection points are also found on the straight wall side of the velocity peak in a region between $x/H \approx 5$ and 10. The inflectional profile on the low-velocity side of the diffuser eventually leads to a recirculating region with flow reversal near the inclined wall. The recirculation region, indicated with the solid line in figure 5, starts at $x/H = 7.4$ and extends to $x/H \approx 30.5$. A maximum backflow velocity of approximately $0.1U_b$ is found around $x/H = 21$. After reattachment there is a slow development of the profiles towards a symmetric shape although the most downstream of the presented profiles is still asymmetric.

The wide and strong shear layer below the backflow region in figure 5 is the major producer of turbulence energy as it interacts with the incoming turbulence from the channel flow. All the non-zero components in the Reynolds stress tensor ($\overline{uu}$, $\overline{vv}$, $\overline{ww}$ and $\overline{uv}$) have their maxima within this shear layer.
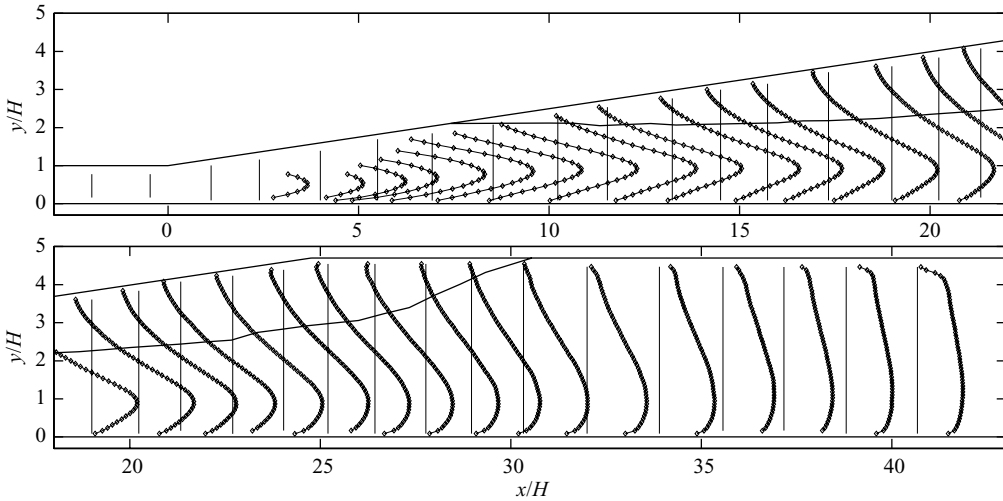
FIGURE 5. Streamwise mean velocity $\left(U_{\text{fig}} = 5U/U_b + x/H\right)$. The vertical lines indicate zero level for each streamwise velocity profile and a solid contour indicates the location of the dividing streamline.
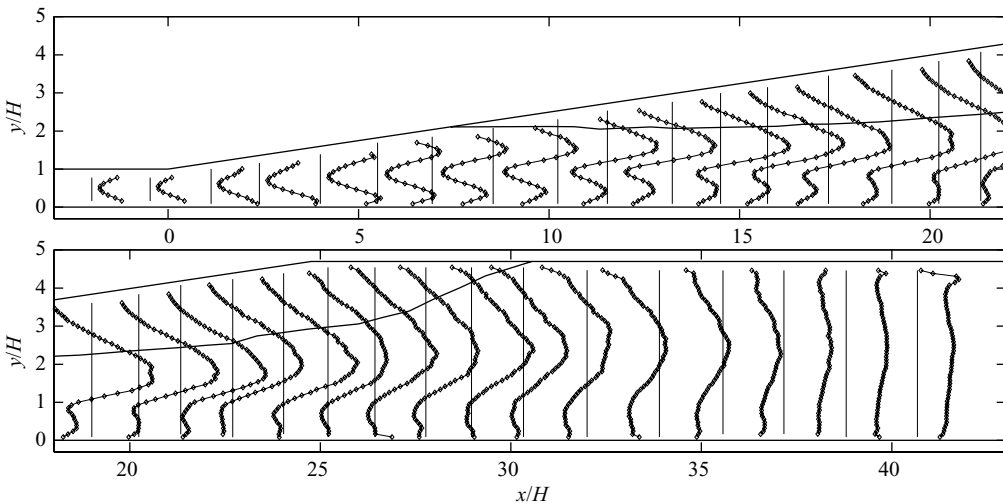

FIGURE 6. Variance of the streamwise fluctuating velocity $\left(\overline{uu}_{\text{fig}} = 200\overline{uu}/U_b^2 + x/H\right)$.

The fluctuating streamwise velocity, shown in figure 6, is in general very large in this flow. The fully developed turbulent inlet flow generates a $\overline{uu}$ distribution that is symmetric, with peaks close to each wall and a local minimum at the centreline where the streamwise velocity gradient is zero. The development of these two peaks is rather different as the flow propagates downstream through the diffuser. The peak close to the straight wall is eventually almost overtaken by the growing local maximum emerging from the upper part of the inlet channel. This peak grows and reaches its maximum at about $x/H = 20$–25. The location of this peak follows the strong shear layer outside the separated region. Eventually, the fluctuating streamwise velocity reaches an almost flat distribution across the outlet channel with small variations along the profile. As the flow in the outlet channel is developing, a turbulent channel
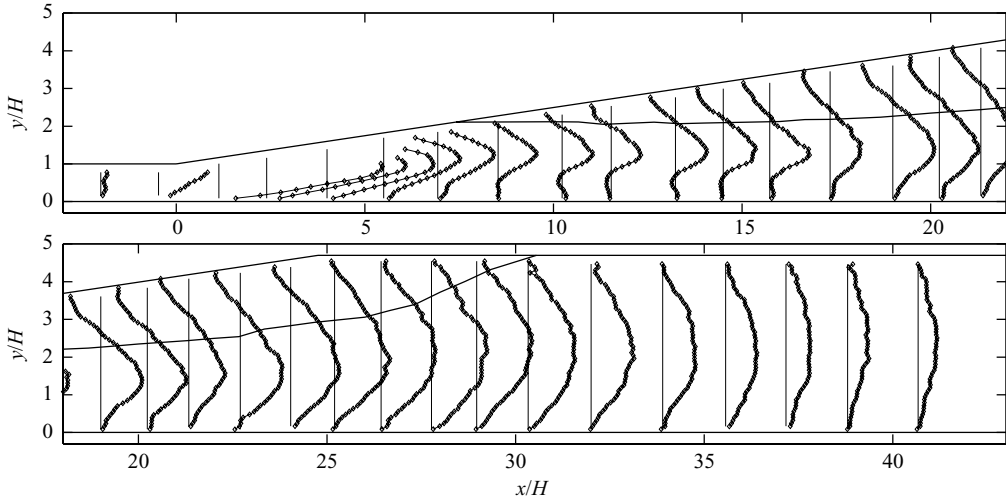
FIGURE 7. Mean velocity in the y-direction $\left(V_{\text{fig}} = 50V/U_b + x/H\right)$.

flow distribution will eventually be recovered far downstream. It can be noted that this channel flow will have the same Reynolds number as the inlet channel flow.

3.1.2. *Mean and fluctuating velocities in the y-direction*

As the velocity in the y-direction, V, is very small in most parts of the diffuser, one can estimate that V is typically at least 10 times smaller than U by comparing the scale factors of the profiles in figures 5 and 7. Close to the corner at the diffuser inlet, where the rather abrupt change in the direction of the wall causes the flow to turn, locally high values of V are found; see figure 7.

Several con clusions regarding the mean flow can be drawn from the V-profiles, bearing in mind the direct relation between velocity gradients $(\partial V/\partial y = -\partial U/\partial x)$ following from the continuity equation. It can be seen that the positions of maximum positive gradient of V correspond to the positions of maximum velocity in U, which means that the deceleration of U is largest at its peaks. The small regions of negative slopes in the V-profiles near the plane wall between $x/H = 10$ and 15 indicate that U is increasing in the x-direction here, most probably due to diffusion of momentum from the region of high velocity above.

Relatively large values of negative V are found near the inclined wall in the recirculation region. This is due to the backflow and the slope of the wall. The centre of the recirculating motion can be estimated by examining where $V = 0$ coincides with $U = 0$. This point is located around $x/H = 23$ and $y/H = 3.3$.

After reattachment, V is positive over the whole exit channel with profile maxima near the centre, reflecting the development of the U-profiles towards a symmetric channel flow.

In the beginning of the diffuser, the fluctuations in the y-direction $\overline{vv}$, shown in figure 8, behave much like the streamwise fluctuating velocity with peaks on both sides of the centreline in the inlet channel followed by a growth of the peak closest to the inclined wall and a reduction of the other peak as the flow propagates in the diffuser. However, the $\overline{vv}$-peak near the straight wall disappears at an earlier x-position as compared to its counterpart in the streamwise direction, $\overline{uu}$. This can be seen as an indication that both the turbulence length scale and its magnitude are
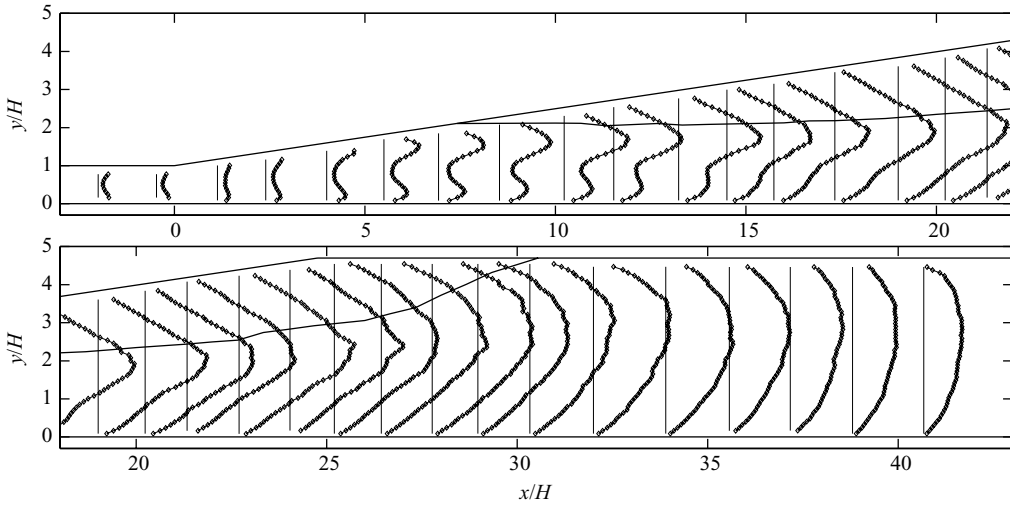
FIGURE 8. Variance of the fluctuating velocity in the y-direction $\left(\overline{vv}_{\text{fig}} = 400\overline{vv}/U_b^2 + x/H\right)$.
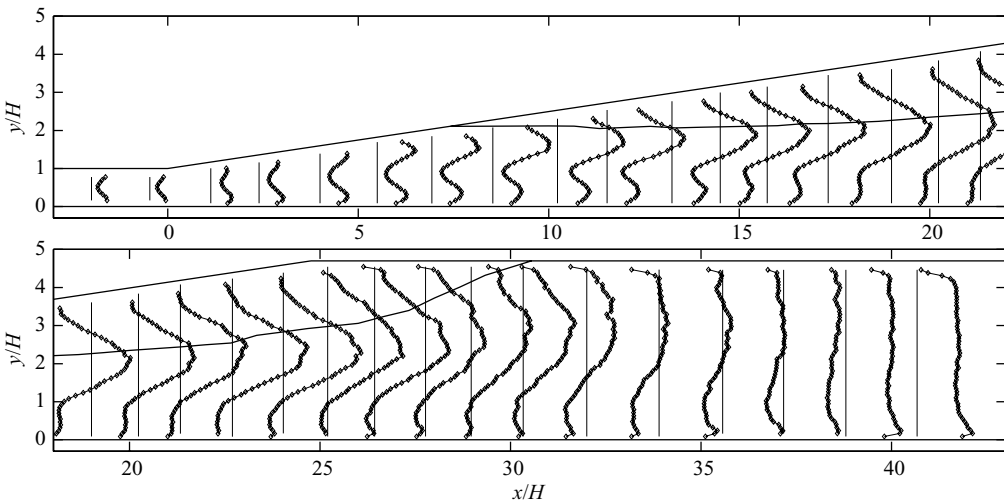

FIGURE 9. Variance of the spanwise fluctuating velocity $\left(\overline{ww}_{\text{fig}} = 400\overline{ww}/U_b^2 + x/H\right)$.

increasing rapidly in the region between $x/H = 10$ and 25, and that $\overline{vv}$ is damped over a larger distance by the presence of the wall. Downstream of $x/H = 25$, the $\overline{vv}$-profiles have similar shapes, while their magnitude is decreasing with increasing x.

3.1.3. *Spanwise fluctuations*

The average velocity in the spanwise direction is considered to be negligibly small, and the global average of the absolute value of W is equal to $10^{-3}U_b$, more than 170 times smaller than the same quantity for the streamwise velocity.

The development of the spanwise velocity fluctuations, $\overline{ww}$, shown in figure 9, resembles very much its streamwise counterpart. The main difference lies in the smaller magnitude of the spanwise component. The y-position of the maximum is also slightly different, with the maximum for the spanwise fluctuating velocity closer to the inclined wall, but still within the shear layer outside the separated region. The
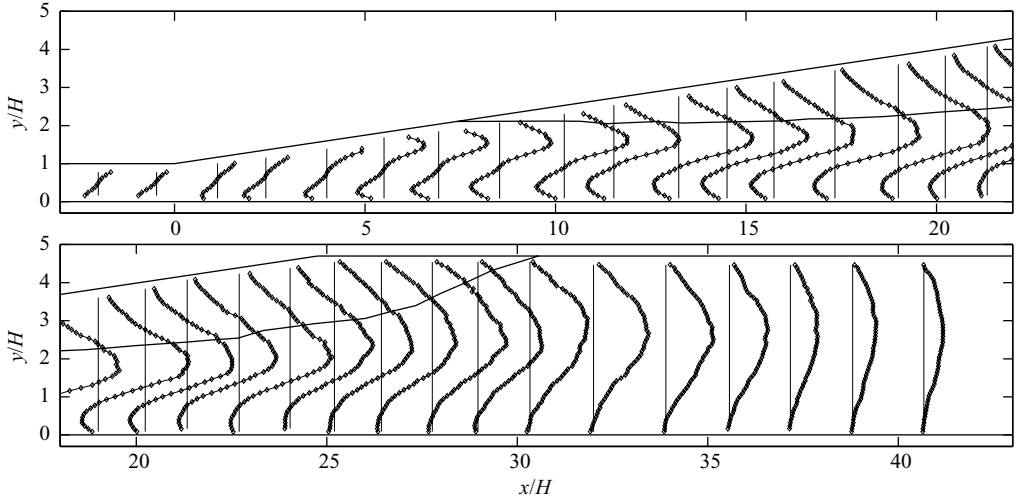
FIGURE 10. Reynolds shear stress $\left(\overline{uv}_{\text{fig}} = 400\overline{uv}/U_b^2 + x/H\right)$.

production term in the transport equation for this component is zero in this flow, since $W = 0$, hence $\overline{ww}$ gains all its energy from the other turbulence components via the pressure–strain rate term. The maximum levels of $\overline{ww}$ are found at $x/H = 20$–25, which is similar to that for the other normal Reynolds stresses.

3.1.4. *Reynolds shear stress*

The Reynolds shear stress is a very important quantity since it redistributes momentum from high-velocity regions to low-velocity regions. The Reynolds shear stress in the xy plane is antisymmetric in the inlet channel (for simplicity, we here show $\overline{uv}$ although the Reynolds shear stress is actually $-\rho\overline{uv}$). As the flow develops downstream in the diffuser, the positive peak grows while the negative peak is suppressed; see figure 10. The maximum magnitudes of $\overline{uv}$ are found at $x/H = 20$–25 and thereafter $\overline{uv}$ decreases. The location of the positive peak follows the location of maximum shear in the shear layer outside the separated region. At the end of the measurement region, $\overline{uv}$ attains an almost symmetric profile with a maximum located near the outflow channel centreline.

No change of sign is visible for $\overline{uv}$ in the region of backflow, where the mean velocity gradient changes sign. This could be a consequence of the lack of near-wall data points, but judging from the slope and magnitude of the profiles in this region it seems quite likely that no sign change occurs. The question whether $\overline{uv}$ changes sign or not is relevant for turbulence modellers since the predicted sign of the Reynolds stresses is directly related to the sign of the mean velocity gradient in many turbulence models.

The Reynolds shear stress $\overline{uv}$ is mainly positive in the exit channel, except for a narrow region close to the straight wall. One can understand the character of these curves from the fact that $\partial U/\partial y$ has the same sign from the upper wall down to about $y/H = 1$. Thereafter, the slope of U is very small except in a narrow region close to the lower wall.

3.2. *Magnitude and production rate of turbulent kinetic energy*

The turbulent kinetic energy, K, is a primary quantity for comparison with turbulence model predictions since most models rely on transport equations for this quantity
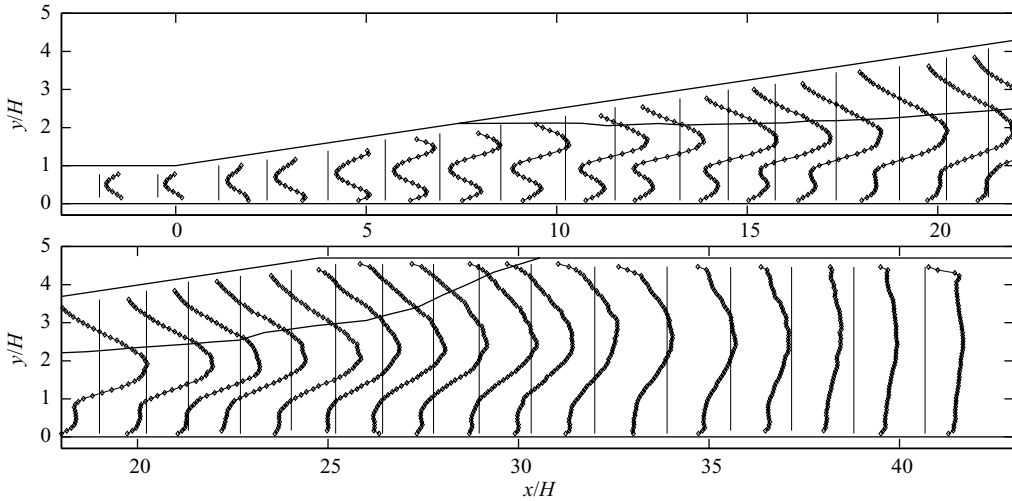
FIGURE 11. Turbulent kinetic energy $\left(K_{\text{fig}} = 200K/U_b^2 + x/H\right)$.

where one or more terms have to be modelled. The turbulent kinetic energy shown in figure 11 is for natural reasons similar in character to the individual intensities shown in previous figures. It is defined as

$$K = \tfrac{1}{2}\left(\overline{uu} + \overline{vv} + \overline{ww}\right). \tag{3.3}$$

The maximum value is, as for the individual fluctuating components, located at about $x/H = 20\text{--}25$ in the shear layer outside the separated region.

The production rate of turbulent kinetic energy

$$\mathscr{P} = -\overline{u_i u_j}\frac{\partial U_i}{\partial x_j} \tag{3.4}$$

is shown in figure 12. The profiles of the production rate are in many aspects similar to those of the produced quantity. Directly after the diffuser inlet, two large production peaks form along each wall. The peak closest to the inclined wall grows both in magnitude and width as we go downstream, while the peak near the straight wall diminishes. A difference as compared to the profiles of the Reynolds stresses is that the maximum value of the production rate is reached around $x/H = 10$, quite far upstream the positions of maximum Reynolds stresses. From $x/H = 10$ and downstream, the dominant peak widens and decreases in magnitude, and after reattachment comparatively little turbulence is produced.

Close to the wall in the downstream of the separated region, small values of negative $\mathscr{P}$ are found. Negative production rates imply that the mean flow is gaining energy from the turbulence; this can occur when turbulence that have formed in a region with a certain strain state is transported to a region with a different strain state. In the plane asymmetric diffuser, negative production of turbulent kinetic energy occurs mainly because the normal stress contribution to the production rate, $-(\overline{uu} - \overline{vv})\partial U/\partial x$, becomes negative near reattachment. However, the shear stress part of the production rate, $-\overline{uv}(\partial U/\partial y + \partial V/\partial x)$, also becomes negative very close to the wall in the same region. The importance of negative production for the mean-reversed flow is discussed and investigated by Törnblom (2006).
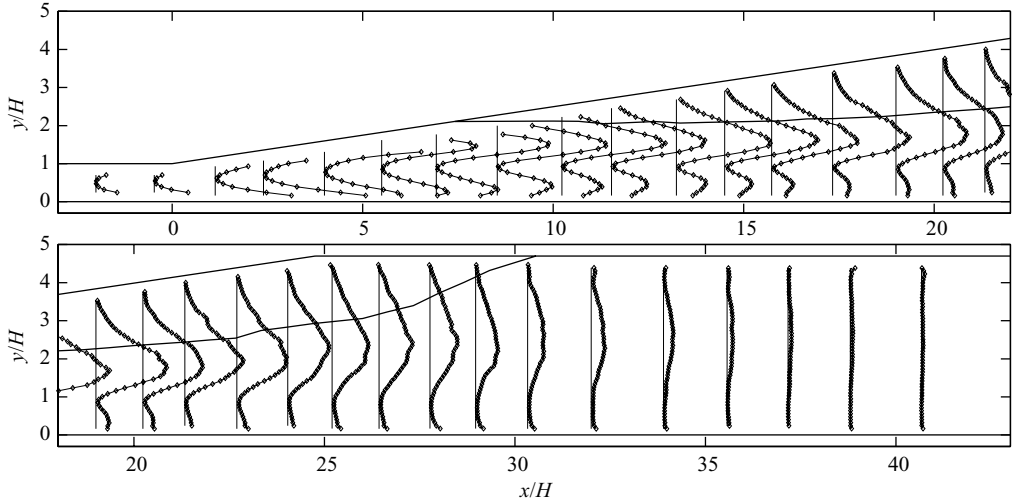
FIGURE 12. Production rate of turbulent kinetic energy $\left(\mathscr{P}_{\mathrm{fig}} = 1000\mathscr{P}H/U_b^3 + x/H\right)$.

3.3. *Characterisation of the separated region*

To study the separated region further, extending the information gained by looking at the velocity profiles, the stream function and the backflow coefficient are useful tools.

3.3.1. *Stream function*

The stream function is defined as

$$\Psi(x, y) = 1 - \frac{1}{HU_b} \int_0^y U(x, y)\,\mathrm{d}y. \tag{3.5}$$

In figure 13, constant values of the stream function (streamlines) are plotted in a region around the separation point. The above definition of the stream function gives a value of $\Psi = 0$ at the dividing streamline. The dividing streamline that separates the (averaged) recirculation zone from the outer flow is included in many of the previously shown profile plots, e.g. figure 5, and is indicated with a thicker line in figure 13. The two positions where the dividing streamline reaches the wall are the mean separation and reattachment points, respectively. From the finer resolution measurements in figure 13, the mean separation point is found to be located at 7.4 channel heights downstream the diffuser inlet ($x/H \approx 7.4$). The mean reattachment point, determined from the coarser data set, is located at $x/H \approx 30.5$. The contours in figure 13 may seem somewhat uneven, but they are computed directly from the raw average velocity field without any prior smoothing and the velocities determining the shape of the dividing streamline are typically 3–4 orders of magnitude smaller than the maximum velocities measured in the same image.

The determined separation point position should be accurate within $\pm 0.1H$ considering the detailed measurements performed in this region. The position of the reattachment point has not been determined with the same precision, and it was taken from the coarse data set as the mid position between the two measurement positions in the x-direction where U changes sign. Due to integration over the interrogation areas, it is more probable that the reattachment position is underestimated than
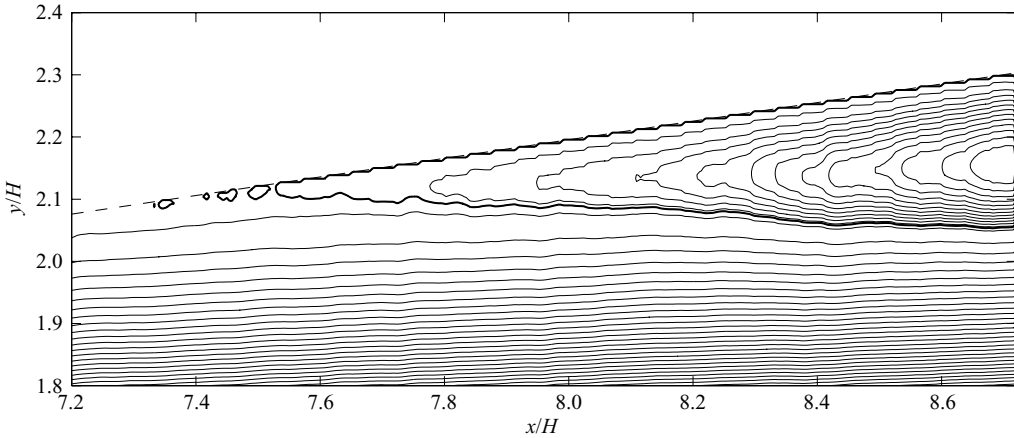
FIGURE 13. Streamlines around the separation point. The dividing streamline, $\Psi = 0$, is shown with a thicker line.

overestimated, since the height of the separation bubble will become thinner than the interrogation area before reattachment.

The angle of the dividing streamline as it detaches from the wall at the separation point is interesting from a turbulence modelling point of view as many models have been seen to give separation bubbles that are very thin at a relatively long distance downstream the point of vanishing wall shear stress followed by a rather abrupt growth of the bubble height. The angle between the wall and the measured separation streamline in figure 13 appears to be smaller near the separation point than farther downstream, but it does not support the turbulence model results that there should be a long thin region of mean backflow before the bubble height starts to increase faster.
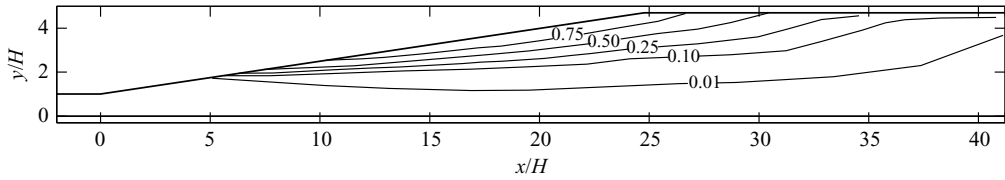
3.3.2. *Backflow coefficient*

An interesting and useful quantity is the backflow coefficient, which relates the number of samples with negative velocity (along the inclined wall) to the total number of samples. A backflow coefficient of one means that all samples have negative velocity, and a backflow coefficient of zero means that all samples have positive velocity. The backflow coefficient then reads

$$\chi(x, y) = \frac{1}{N} \sum_{k=1}^{N} \frac{1 - \text{sgn}\left[u_k(x, y)\cos(\alpha) + v_k(x, y)\sin(\alpha)\right]}{2}, \tag{3.6}$$

where N is the total number of samples, sgn is the sign function, u_k is the streamwise velocity in the kth sample, v_k is the y-direction velocity in the kth sample and $\alpha = 8.5°$ is the diffuser opening angle.

First, we notice in figure 14 that along the straight wall there seems to be no samples with backflow. It is important that there is no separation on the straight wall since this may destroy the 'stability' of the separation bubble on the inclined wall with a separation-altering side from the inclined wall to the straight wall back and forth.

The backflow coefficient in figure 14 shows that the most upstream point for instantaneous flow reversal is found at $x/H \approx 5$. The flow is separated $>75\%$ of the time downstream at $x/H \approx 11$. The contour of $\chi = 0.5$ should, according to available data from other separating flows, coincide with the mean dividing streamline at the

FIGURE 14. Backflow coefficient χ.

points of separation and reattachment (Simpson 1989). This was checked for and found to be true in both the fine resolution and coarser measurements. Nowhere in the diffuser was backflow found in $> 90\,\%$ of the samples. However, this does not necessarily imply that the flow is fully attached everywhere in the diffuser at some instances of time. It merely says that occasionally the instantaneous flow is in the streamwise direction also near the inclined wall but nothing about the spatial extent of the particular events. Following the $\chi = 0.01$ contour in figure 14 where $99\,\%$ of the samples are in the streamwise direction, we find that while being limited to a rather short region upstream the mean separation point, instantaneous flow reversal may occur far downstream the mean reattachment point. This behaviour is probably caused by turbulence structures that have velocity scales larger than the mean velocity downstream the reattachment point. These are created over the separated region and then advected downstream.

3.4. *Static wall pressure distribution*

The static wall pressure has been measured along the spanwise centreline in the downstream direction. Measurements on both the inclined and straight walls were performed but with a much better spatial resolution on the straight wall. The measurements on the inclined wall showed that the static pressure is equal on the two sides, for constant x (within our measurement accuracy), with an exception for the upstream corner where the rapid change in wall direction leads to strong curvature of the streamlines and consequently pressure differences between the two sides.

Figure 15 shows the pressure coefficient, C_p, defined as

$$C_p(x) = \frac{p_w(x) - p_w(x = 0)}{\frac{1}{2}\rho U_b^2}, \tag{3.7}$$

where p_w is the static wall pressure on the straight wall and ρ is the density of the air. The adverse pressure gradient is strongest in the beginning of the diffuser and diminishes in the downstream direction until $x/H \approx 13$ where a region with nearly constant pressure gradient is reached. This straight region is caused by the constriction to the flow through the diffuser constituted by the recirculation region. The pressure gradient increases slightly in the reattachment region of the separation bubble.

The effect of the boundary-layer suction applied at the endwalls (see §2.1) is that the flow is slightly expanded in the spanwise direction. This can be observed in the C_p-measurements at $x < 0$ where the expected negative slope of the curve cannot be observed.

3.5. *Conservation of mass*

Integration of the U-velocity profiles in the y-direction gives a measure of the flow rate through the diffuser at different x-positions. Ideally, the flow rate

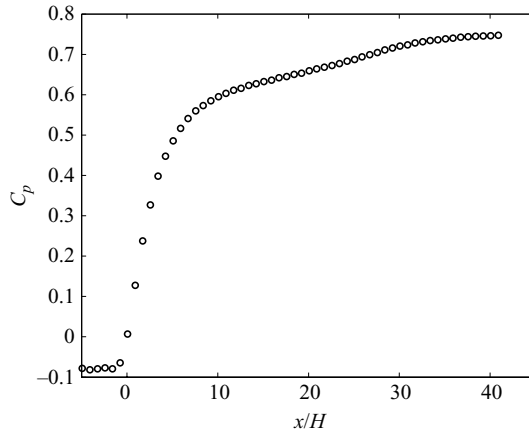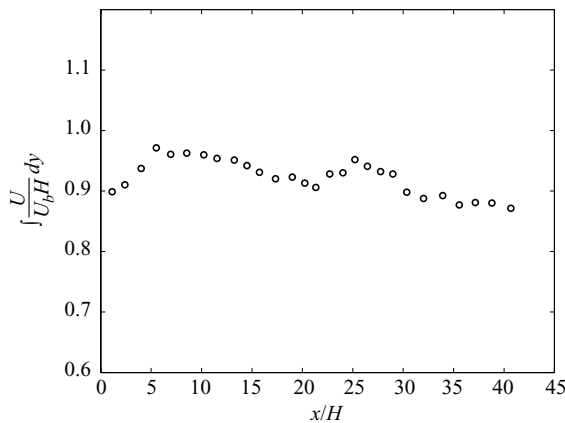$$\int_{bottom}^{top} \frac{U}{U_b H}\mathrm{d}y \tag{3.8}$$

FIGURE 15. Static wall pressure coefficient, C_p, along the straight diffuser wall.

FIGURE 16. Integrated flow rate.

would be constant equal to unity for flawless measurements of a perfectly two-dimensional flow. However, figure 16 shows that the measured flow rate is smaller than unity for all profiles. This deficiency can be attributed to the omission of the near-wall measurement points, as explained in §3.1. The numerical integration was done using the trapezoidal rule and the velocity profiles were approximated to straight lines between the wall and the measurement point closest to the wall. Comparisons with DNS data yield that the bulk velocity in the flow near the inlet may be underestimated by approximately 4 %. There is also an effect of the boundary-layer suction applied upstream the inlet, causing an overestimation from Deans formula that is estimated to be roughly 4 %. These two factors explain the major part, but not completely, the low value (0.90) for the normalized local bulk velocity at $x = 0$. Taking this into consideration, the remaining deviation of the measured flow rate from an ideal two-dimensional flow is in the range of 2 %–5 %.

Separation on the diffusers endwalls, which is a known problem in this type of flow geometry (see e.g. Buice & Eaton 1997; Kaltenbach *et al.* 1999; Obi *et al.* 1999), would result in a flow rate that is increasing in the streamwise direction along the diffuser centreline. Such trends cannot be seen in the present measurements. A weak
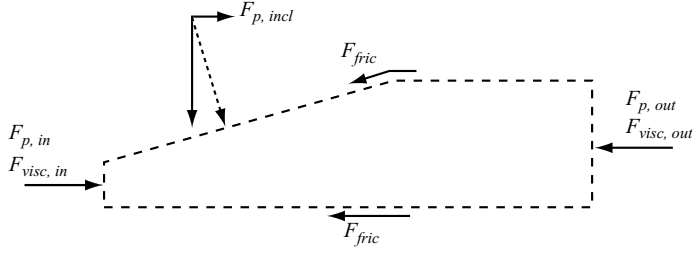
FIGURE 17. Forces acting on a control volume in the diffuser.

trend is instead seen towards lower flow rates for larger values of x. No feasible explanation has been found for this trend, other than that the insufficient near-wall resolution of the integrated profiles gives a general uncertainty of the integrals.

3.6. *Momentum balance*

Being a two-dimensional flow confined between two walls, the consistency between the measured forces on a control volume and the measurements of the resulting momentum flux change can be readily investigated. The x-momentum flux change $\Delta M_x = M_x(x_{out}) - M_x(x_{in})$ between two cross-sections at $x_{in} = 0$ and x_{out} is related to the forces acting on the control volume as

$$\Delta M_x = (F_{p,in} - F_{p,out} + F_{p,incl}) + (F_{visc,in} - F_{visc,out}) - F_{fric}. \qquad (3.9)$$

Figure 17 shows how the different forces act on the control volume. Being a two-dimensional flow all quantities are per unit length in the spanwise direction. The pressure forces acting on the inlet or outlet cross-sections and in the x-direction on the inclined wall are defined as

$$F_{p,x} = \int_{bottom}^{top} P(x, y)\mathrm{d}y \quad \text{and} \quad F_{p,incl} = \int_{in}^{out} P(s)\sin(\alpha(s))\mathrm{d}s, \qquad (3.10)$$

respectively. The second integral is evaluated along the walls and $\alpha(s)$ is the angle between the x-axis and the wall. The skin friction and viscous forces are defined as

$$F_{visc,x} = \int_{bottom}^{top} -\mu\frac{\partial U}{\partial x}\mathrm{d}y \quad \text{and} \quad F_{fric} = \int_{in}^{out} \tau_w \cos(\alpha(s))\mathrm{d}s, \qquad (3.11)$$

where μ is the dynamic viscosity and τ_w is the wall shear stress. The momentum flux through a vertical cross-section is given by

$$M_x(x) = \int_{bottom}^{top} \rho(U^2 + \overline{uu})\mathrm{d}y. \qquad (3.12)$$

With the present experimental data set, the pressure was taken to be constant over the cross-sections equal to the static pressure at the straight wall. The errors due to this approximation should be small, considering that the measured pressure is equal on both walls for the same x-position (cf. §3.4). The interior pressure distribution over the cross-sections can be computed by integrating the y-momentum equation; however, this will change $F_{p,x}$ by less than 1%. The viscous forces are small at the present Reynolds number and are thus not considered in the analysis of the momentum balance. Measurements of the wall shear stress has not been made in the present experiment and the frictional forces cannot, therefore, be included in the balance, the implication of which will be discussed later.
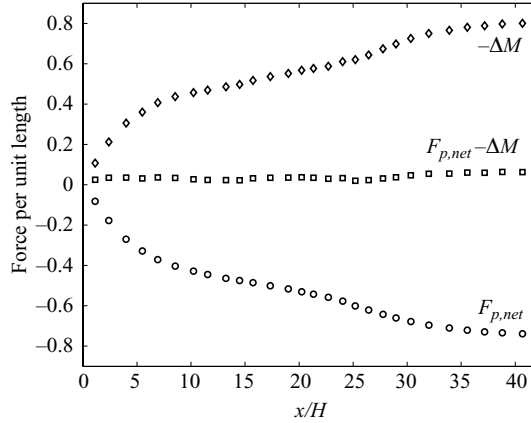
FIGURE 18. Terms in the momentum balance equation, $F_{p,net} = F_{p,in} - F_{p,out} + F_{p,incl}$. The data are normalized by $(\rho H U_b^2)$.

Figure 18 illustrates the balance between the left- and right-hand sides of (3.9). It is seen that the pressure forces are, by far, the largest contributors to the change in momentum. The residual visible in the middle curve of figure 18 can probably to a large extent be attributed to the neglected skin-friction term in (3.9), which according to Kaltenbach *et al.* (1999) accounts for approximately 5 % of the momentum balance in the similar 10° diffuser case.

3.7. *Energy balance*

Using tensor notation, the Reynolds-averaged transport equation for the mean flow kinetic energy $Q = \rho U_i^2/2$ may be written as

$$\frac{\partial}{\partial x_j}(U_j Q) = -\frac{\partial}{\partial x_j}\left(U_j P + \rho U_i \overline{u_i u_j}\right) + U_i \frac{\partial}{\partial x_j}\left(\mu \frac{\partial U_i}{\partial x_j}\right) + \rho \overline{u_i u_j} \frac{\partial U_i}{\partial x_j}. \tag{3.13}$$

The last term is a source term that is usually negative, transforming mean kinetic energy to turbulence. The term is identical to the production term in the transport equation for the turbulent kinetic energy, but with opposite sign. By integrating (3.13) over a control volume extending across the diffuser in the y-direction and from $x_{in} = 0$ to x_{out} and using Gauss' theorem, we arrive at the expression

$$\mathscr{P}^{tot} = -\left(E_m^{tot}(x) - E_m^{tot}(0)\right) + \int_{x_{in}}^{x_{out}} \int_{bottom}^{top} \mu\left(U\nabla^2 U + V\nabla^2 V\right) dx\, dy, \tag{3.14}$$

where

$$\mathscr{P}^{tot} = \int_{x_{in}}^{x_{out}} \int_{bottom}^{top} \rho \mathscr{P}(x, y)\, dy\, dx \tag{3.15}$$

is the total rate of production of turbulent kinetic energy and

$$E_m^{tot}(x) = \int_{bottom}^{top} (U(x, y)(P(x, y) + Q(x, y) + \rho\overline{uu}(x, y)) + V(x, y)\rho\overline{uv}(x, y))\, dy \tag{3.16}$$

can be interpreted as a flux of mechanical energy over a cross-section. Both E_m^{tot} and $\mathscr{P}^{tot}$ are given per unit depth in the spanwise direction. Here, E_m^{tot} will diminish through the diffuser as the mean kinetic energy is transformed into turbulent kinetic
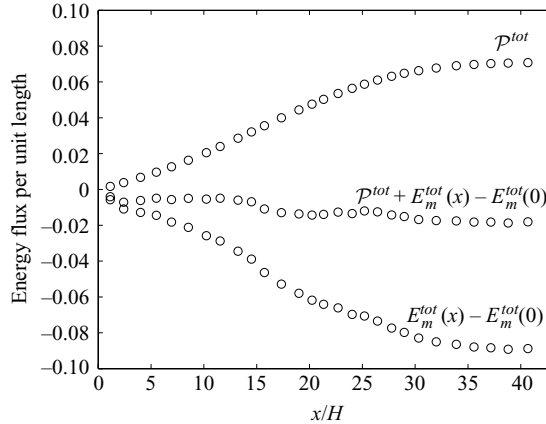
FIGURE 19. Mechanical energy of the mean flow (the lower curve), $\mathcal{P}^{tot}$ between $x_{in} = 0$ and $x_{out} = x/H$ (the upper curve) and their residual (the middle curve). The data are normalized by $\rho H U_b^3$.

energy and heat. There are two paths that the mechanical energy drained from the mean flow can take: either it can be transformed to turbulent energy or it can be directly transformed into heat by viscous dissipation due to the mean flow gradients.

The loss of mechanical energy from the mean flow from $x_{in} = 0$ and downstream is shown in the lower curve of figure 19. The loss at the most downstream measurement station amounts to approximately 15 % of the available mechanical energy of the mean flow at the diffuser entrance. The upper curve in figure 19 shows the total amount of energy transferred from the mean flow to the turbulence from $x_{in} = 0$, and downstream the resemblance of the upper and lower curves shows that the main path taken by the energy drained from the mean flow is through transformation into turbulence. The middle curve in figure 19, showing the residual between the upper and the lower curves, represents the losses of mean flow energy due to direct viscous dissipation by mean flow shear.

The non-perfect mass balance (cf. figure 16) can have a small effect on the measured energy balance. However, the fact that the slope of the middle curve in figure 19 is negative nearly everywhere makes it reasonable to assume that the balance is quite accurate.

4. Temporal and structural flow behaviour

Time-resolving PIV is used here to investigate both the formation of a separation in the vicinity of the mean separation point and the evolution of typical structures seen in the spanwise velocity fluctuations. Spatial auto-correlation functions are presented for a number of positions throughout the diffuser.

4.1. *Formation of backflow near the separation point*

In §3.3.1, the position of the separation point was determined at $x/H = 7.4$, and figure 20 shows a time sequence of instantaneous velocity vector fields in a region near this point. The magnitude of the backflow along the inclined wall is indicated with shades of grey, larger magnitude corresponding to brighter shades. From the images we can see that the flow in this region is highly unsteady and that there is a region with relatively low velocity near the wall and a high-velocity region farther
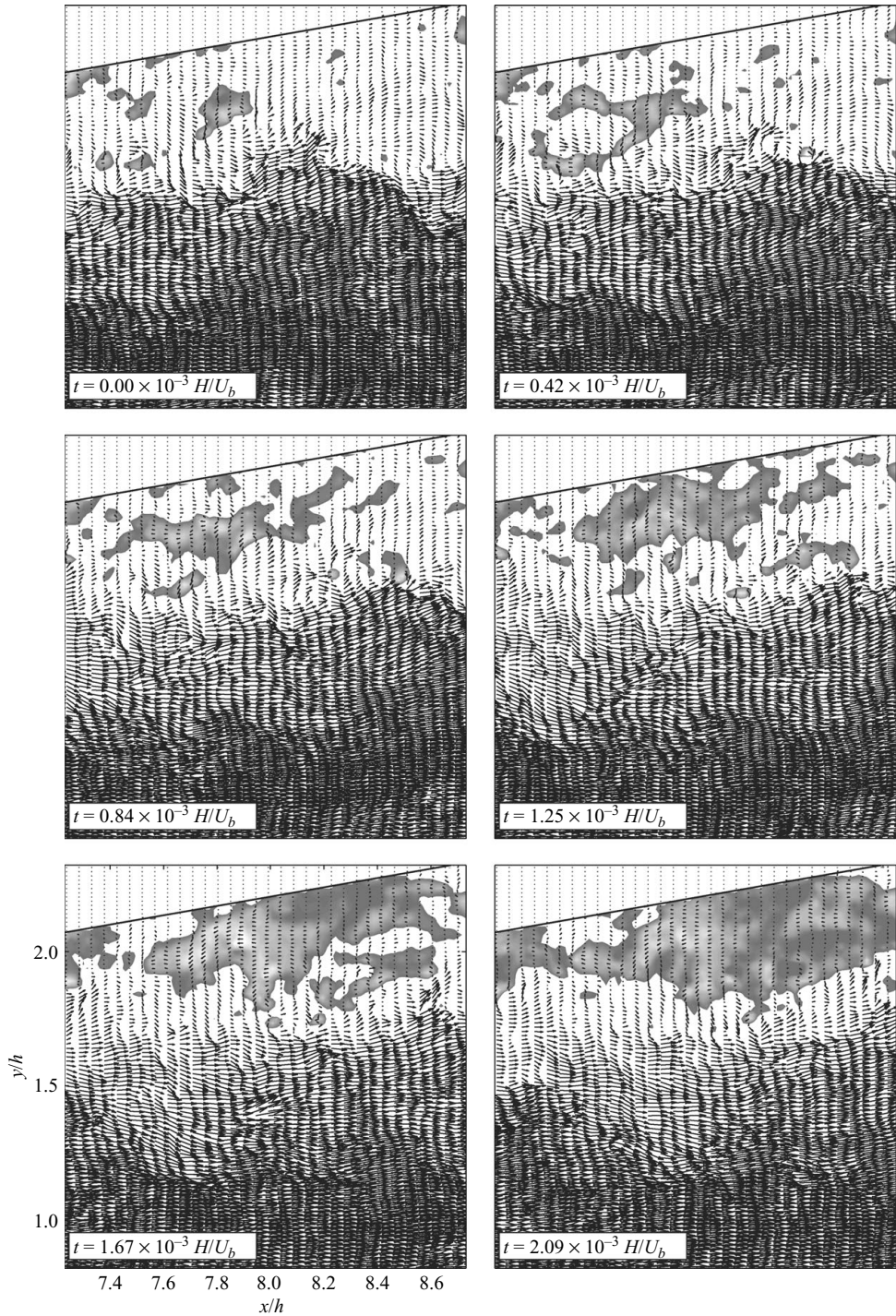
FIGURE 20. Instantaneous vector fields from a region around the mean separation point. The backflow velocity along the inclined wall is displayed by shades of grey, and brighter shades correspond to larger magnitudes of the backflow.

out. The sequence shows the formation of a region of backflow, but it is difficult to distinguish any particular cause for the formation of the backflow region. Judging by the size of the forming backflow region, its cause is likely to be some velocity fluctuation with a quite large length scale; but in figure 20 motion on such scales is somewhat hidden behind velocity variations with smaller length scales and the average flow variations. In an attempt to reveal the large-scale velocity variations, the vector field was bandpass filtered by subtracting the mean flow and filtering the fluctuations with a two-dimensional Gaussian low-pass filter. In figure 21 the result after such an operation is shown, in this particular case the Gaussian filter has a standard deviation of five vectors (it should be noted that every vector in the y-direction is shown in figures 20 and 21, but only every third in the0 x-direction). In figure 21 one can easily see the connection between the regions of backflow and the velocity vectors; however, the formation of the backflow region does not appear to be connected to the passage of a strong vortex. The structure of the large-scale fluctuations appears to be more wave-like than vortex-like. Galilean decomposition instead of Reynolds decomposition of the filtered velocity field does not reveal any large-scale vortices either.

4.2. *Structures of the spanwise velocity fluctuations*

Many of the recorded velocity fields show inclined structures of spanwise velocity fluctuations. The structures come in pairs of one positive and one negative structure and appear to be approximately aligned with one of the principal axes of the mean strain rate tensor. Figure 22 shows a sequence of images where such a pair of structures is convected downstream, stretched and smeared out. In the first image an inclined structure of strong positive (the solid line contours) spanwise velocity can be seen, and gradually a following structure of negative w (the dotted contours) appears in the images. The strength of the positive structure is successively diminishing while the strength of the negative structure increases. The structures also appear to be rotated, or stretched by the flow, towards being horizontal. The structures are eventually smeared out and in the last image the leading positive structure is barely visible. However, another positive structure has appeared now, following the negative structure. In the first five images one can perceive a reducing effect on the region of backflow, indicated by a thicker solid line, from the structures. It is unclear whether this is a general effect.

It is possible that the structures seen form one of the legs of a hairpin- or horseshoe-like vortex and the new structures following the first could be an indication of a hairpin packet proposed by Adrian, Meinhart & Tomkins (2000*b*) to appear in the outer region of turbulent boundary layers.

4.3. *An ejection event and a possible hairpin vortex*

Galilean decomposition of a vector field here simply means to display the field in a moving frame of reference by subtracting the reference frame velocity $[U_G, V_G]$ from the flow velocities. When the velocity of the reference frame matches the velocity of a vortex, the vortex will appear as a roughly circular pattern of velocity vectors (Adrian, Christensen & Liu 2000*a*). The signature of a hairpin vortex in a PIV measurement is described by Adrian *et al.* as a region of strong second quadrant vectors (pointing upstream and outward from the wall) located upstream and on the wall side of the vortex, and the angle of this region should be approximately 45° relative to the wall.

Figure 23 shows a temporal sequence of four Galilean decomposed vector fields, where the reference frame velocity is displayed on the top of each field. In the first image only a quite weak vortex can be distinguished, but the background colour scale
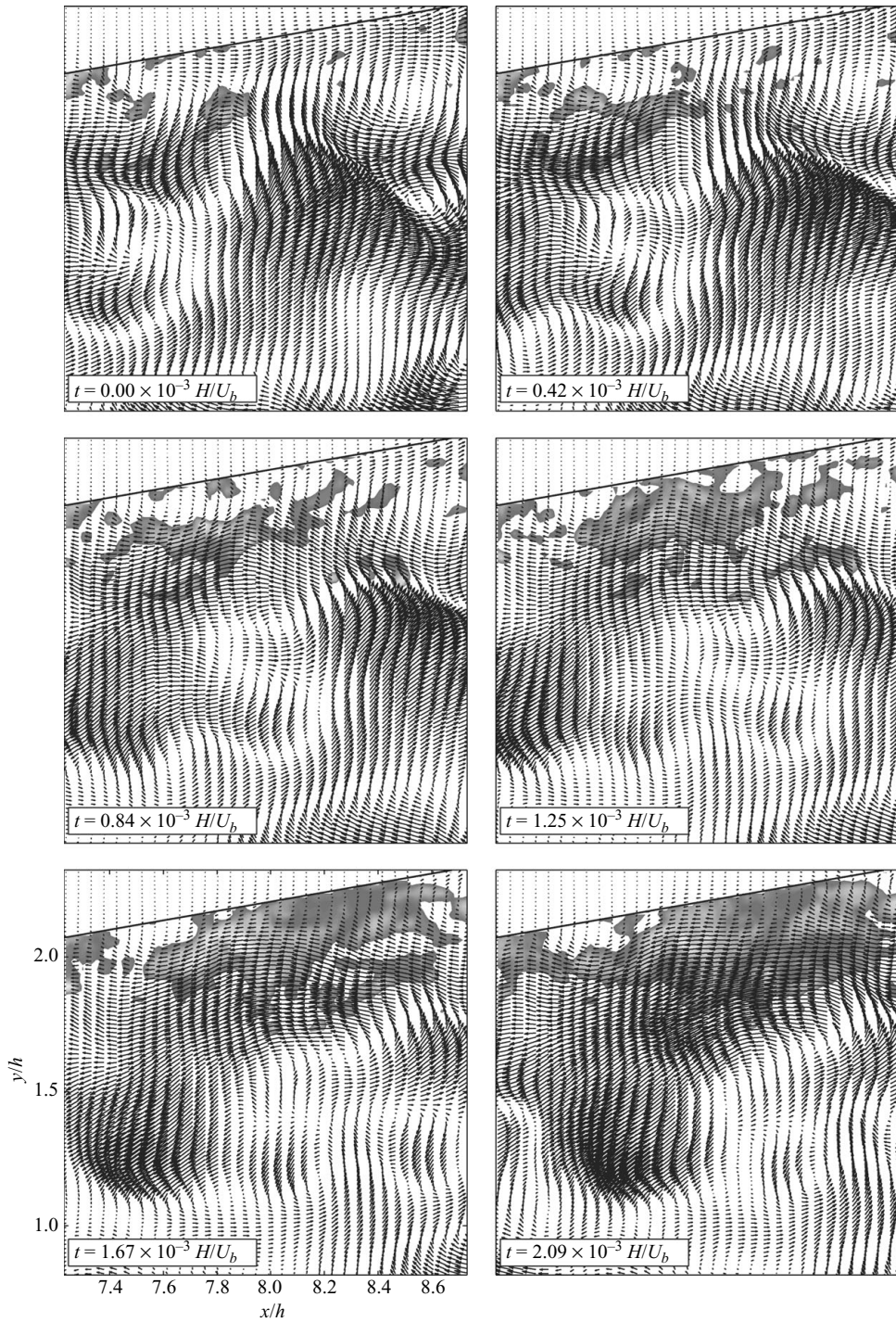
FIGURE 21. Bandpass filtered instantaneous vector fields from a region around the mean separation point. The backflow velocity along the inclined wall is displayed by shades of grey, and brighter shades correspond to larger magnitudes of the backflow.
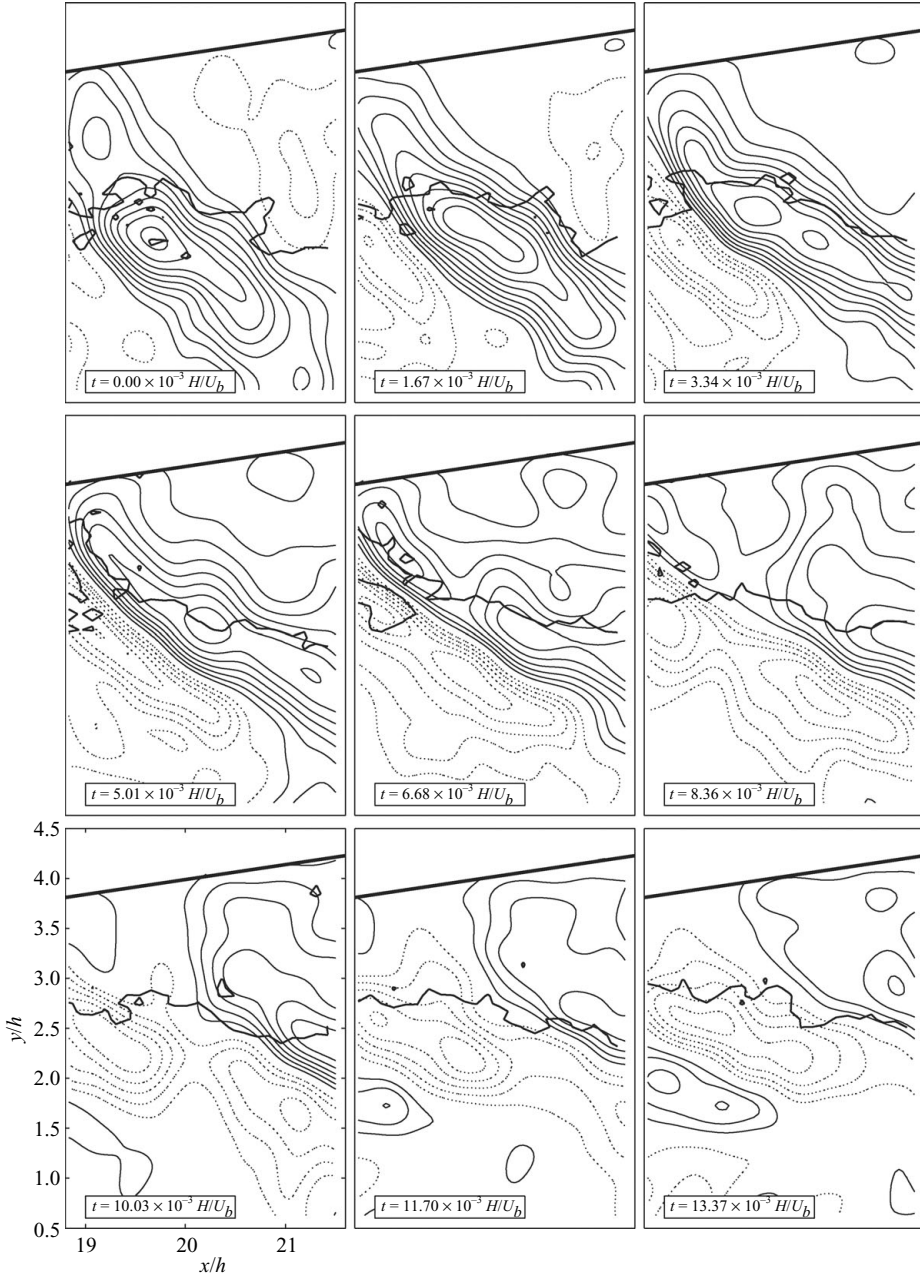
FIGURE 22. Bandpass filtered instantaneous fields of w. The solid line contours are drawn for $w/U_b \geqslant 0.5$ and the dotted contours correspond to $w/U_b \leqslant -0.5$. The increment between contours is 0.5. Contours drawn with a thicker line enclose regions with backflow along the inclined wall.

showing the spanwise velocity, positive being out of the paper plane, indicates that there is an inclined structure of the same character, as those described in §4.2, in the upper left corner of the first image. The vortex seen in the second image is also relatively weak but more aligned with the w-structure. The w-structure has almost
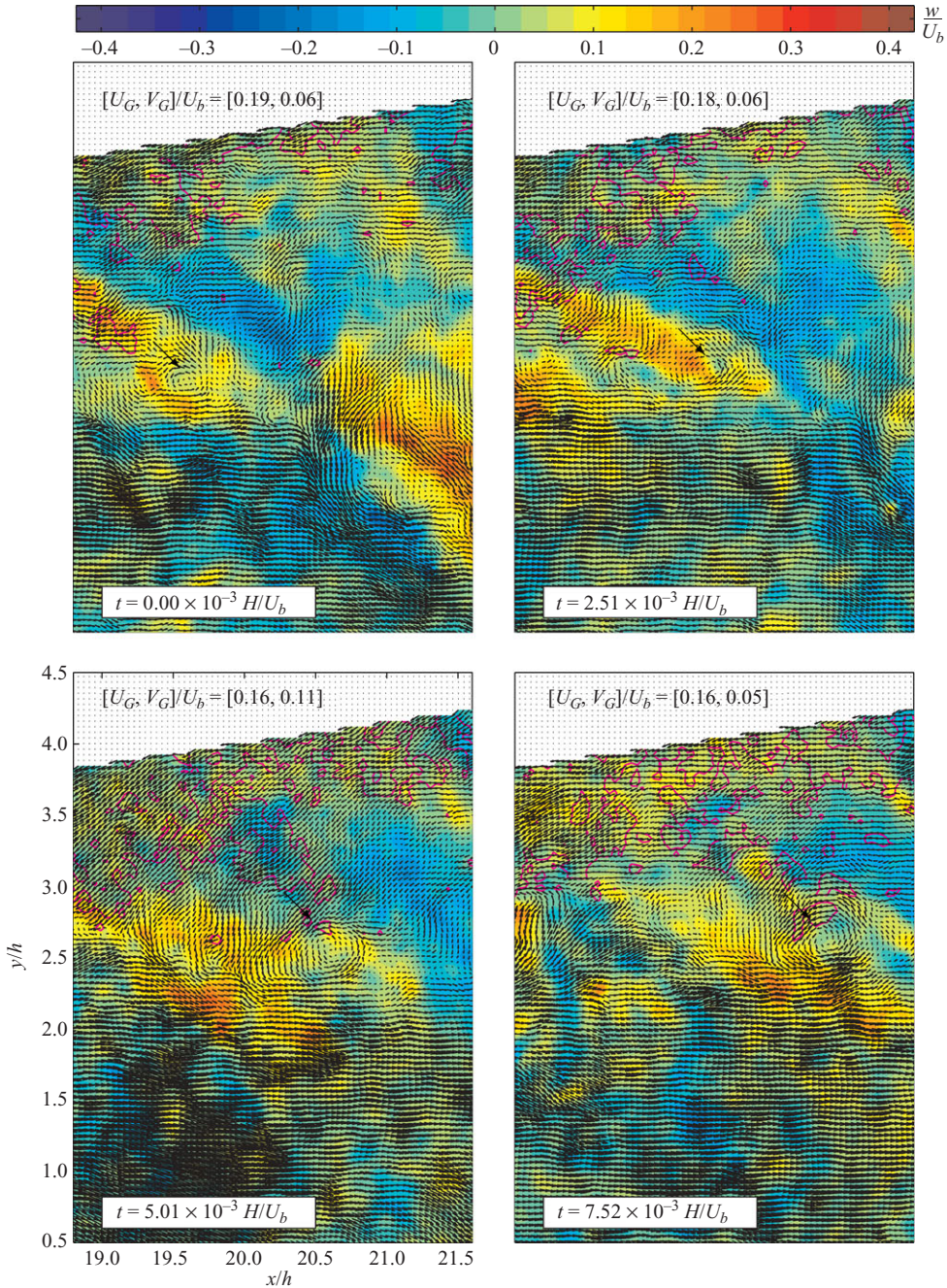
FIGURE 23. Instantaneous vector fields. Background colours show the spanwise velocity (see the colour bar). Magenta contours enclose regions with backflow along the inclined wall. Arrows point out the vortex described in the text.

disappeared in the third image, but here we see instead the signature of a hairpin vortex, a quite strong vortex together with an ejection. The signature of the hairpin vortex can still be seen in the fourth image. Notable is also the increased backflow that seems to be a result of the ejection.

A reasonable explanation of the observed events is that the vortices seen in the first two images are not part of the hairpin vortex and that we instead see a hairpin vortex that in the beginning has its spanwise centre below the measurement plane, but successively moves in the positive z-direction so that its spanwise centre is near the measurement plane in the last two images. A region of positive velocity in the z-direction, not associated with the structures, that could explain the spanwise translation of the hairpin structure can indeed be observed in the images.

4.4. *Spatial spectra*

The spectral analysis of turbulence gives information on how the turbulent fluctuations are distributed over different spatial (or temporal) scales. Computing spatial spectra in a direction where the mean flow is inhomogeneous, as is done here, is somewhat questionable. However, the variation of mean flow velocities and turbulence intensities is relatively small along the lines where the spectra have been evaluated; hence, the average spectral distribution should not be expected to vary considerably along these lines either.

The presented spectra were calculated as

$$E_{ii} = \frac{\hat{u}'_i(kH)\hat{u}'^{*}_i(kH)}{U_b^2}, \tag{4.1}$$

where $\hat{u}'_i(kH)$ is the Fourier transform of the fluctuating velocities measured along a line in space, k is a wavenumber and the asterisk denotes the complex conjugate. The presented spectra have been prepared using the methodology described by Foucaut, Carlier & Stanislas (2004) and should thus not have any significant bias due to noise.

Figure 24 displays spectra for u' and v' computed from two-component measurements near the separation point. In this region the E_{11}-spectra are similar in shape for all the investigated y-positions across the diffuser; the spectra differ only in magnitude, a difference that can be related to the magnitude of $\overline{uu}$ at the different positions. The slopes of the E_{11} spectra are near $-5/3$ for an intermediate range of wavenumbers, indicating that there exists an inertial sub-range between the large- and small-scale turbulence. This inertial sub-range (in figure 24b) seems to be centred around $kH \approx 10$, corresponding to spatial wavelengths of about $0.6H$.

The E_{22} spectra are also rather similar, independent of the y-position, but have less energy at small wavenumbers as compared to the E_{11} spectra. This is, of course, only a reflection of the fact that the $\overline{uu}$ turbulence component has more energy than the $\overline{vv}$ component. At larger wavenumbers though, the energy levels of $\overline{vv}$ are of the same order, or even larger, than those of $\overline{uu}$ (the $k^{-5/3}$ lines are drawn in the same position in the two figures and can be used as a reference). Hence, the turbulence in this region is approximately isotropic at small scales.

The spectra shown in figure 25 are taken along the numbered lines shown in figure 25(a), and globally this region is located just upstream the downstream corner of the diffuser. In this region the turbulent velocities reach their maximum values, the turbulence production however reaches its maximum peak farther upstream (see § 3.2). Most of the E_{11}-spectra shown in figure 25 have a slightly concave shape. This shape can be interpreted as a result of the turbulence not being in local equilibrium with the mean flow and that the relatively large levels of small-scale turbulence are due to turbulence produced elsewhere that have been transported to this spatial region and broken down to smaller scales along the way. This effect is seen in the spectra of all three components at the position closest to the inclined wall where probably a major
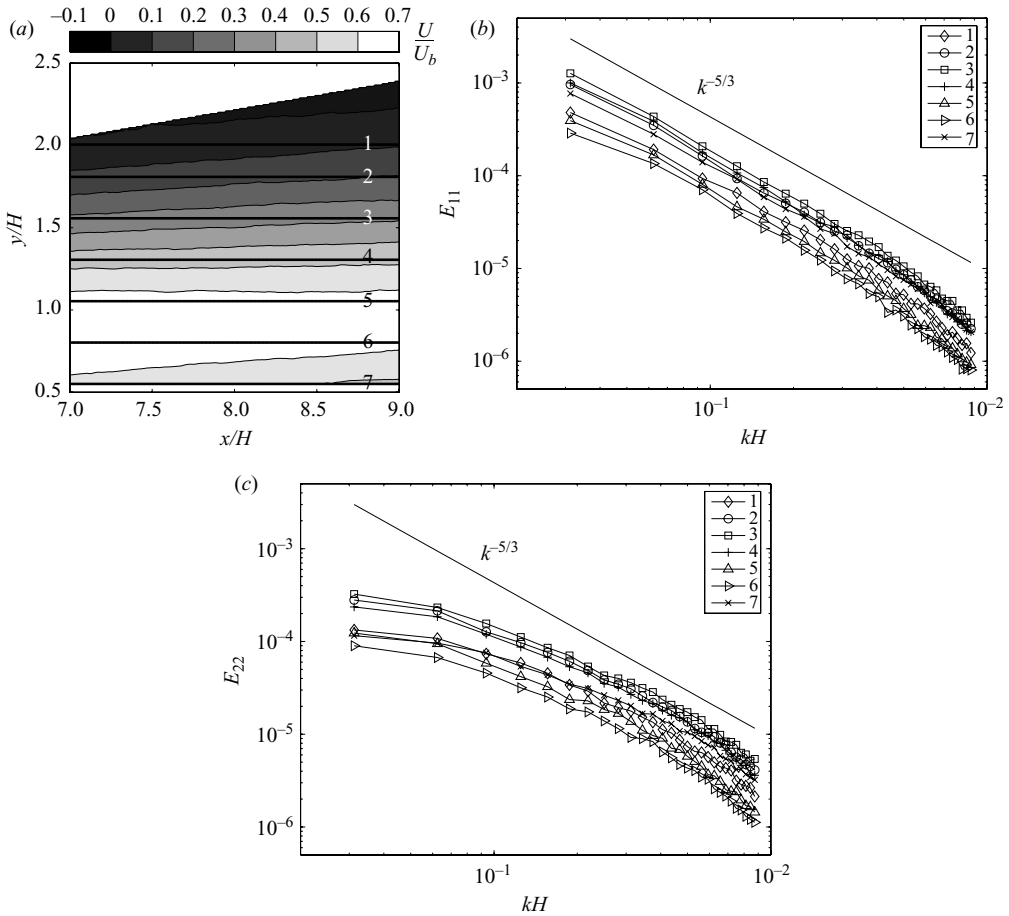
FIGURE 24. Graphs (*b*) and (*c*) show spectra of velocities in the *x* and *y*-directions, respectively. The data were taken along the lines indicated in (*a*). The contours in (*a*) show the mean velocity in the *x*-direction.

part of the turbulence is produced elsewhere since the production rate of turbulence is small in this region.

4.5. *Spatial correlations*

Spatial auto-correlations give an indication of the dominating scale of the velocity fluctuations. The presented correlations are calculated as

$$R_{u_i u_i}(x, y) = \frac{\overline{u_i'(x, y) u_i'(x_0, y_0)}}{\sqrt{\overline{(u_i' u_i'(x, y))}} \sqrt{\overline{(u_i' u_i'(x_0, y_0))}}}, \tag{4.2}$$

where u_i' is the fluctuating velocity in the x_i-direction and (x_0, y_0) are the coordinates of the fixed point around which the correlation is computed.

Figure 26 shows the spatial auto-correlation for the velocities in the streamwise direction, R_{uu}, computed at eight different streamwise stations at heights $y/h(x) = 0.2$, 0.4, 0.6 and 0.8, with $h(x)$ being the local duct height. The figure reveals that the turbulence length scale grows with increasing x in the diffusing part and that the length scale in the exit channel is nearly constant. In the diffusing part, between
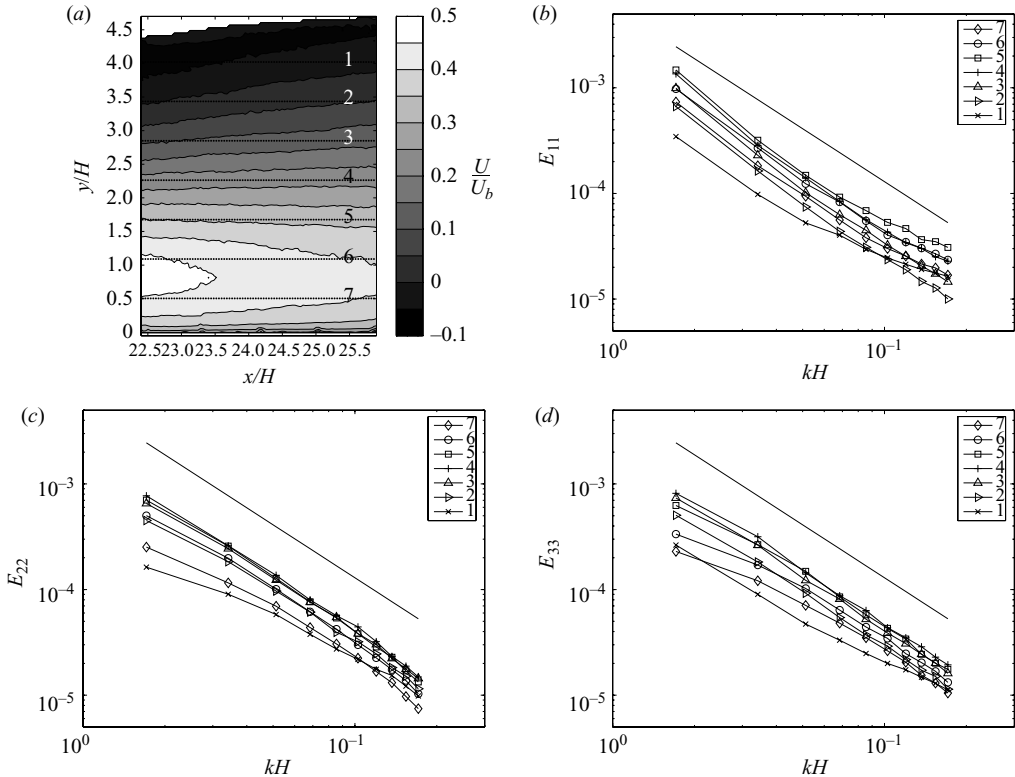
FIGURE 25. Spatial spectra of (b) u', (c) v' and (d) w', computed from data taken at the lines shown in (a).

$x/H \approx 15$ and 25, there are apparent negative correlations between u' in the centre region and u' close to the straight wall, these are likely to be due to the motion of the 'jet-like' high-velocity region emanating from the inlet channel. Early in the diffuser ($x/H = 10$–15), there is a strikingly distinct boundary in the correlations with a y-position in the vicinity of the maximum mean U-velocity and the gradients of the correlation coefficients become very steep as this boundary is approached. The u'-fluctuations in the separated region appear to be rather unaffected by events occurring near the straight wall. It can also be noted that the correlation peaks' main axes are inclined in the first part of the diffuser but become close to horizontal farther downstream. For zero pressure gradient turbulent boundary layers Krogstad & Antonia (1994) report an angle of $\sim 10°$ for the R_{uu} correlation.

The auto-correlations of v', shown in figure 27, also display an increased length scale in the diffusing part and a nearly constant length scale in the exit channel. In general the lengths over which v' is correlated are smaller than for u', and the R_{vv}-peaks are more circular although they are slightly elongated in the y-direction. Negative correlations for this velocity component are primarily seen in the lowest image of figure 27 (where $y_0 = 0.2h(x)$) and are, as for R_{uu}, likely to be due to the motions of the high-velocity region. A rough estimate of the 'wavelength' of this motion based on R_{vv} shows that it is on the order of $5H$.

The peaks of R_{ww}, shown in figure 28, have a pronounced $\sim 45°$ inclined shape, resembling the shape of the structures described in §4.2. Negative correlations are found on both sides of the peaks along the minor axes of the peaks. This shape of the
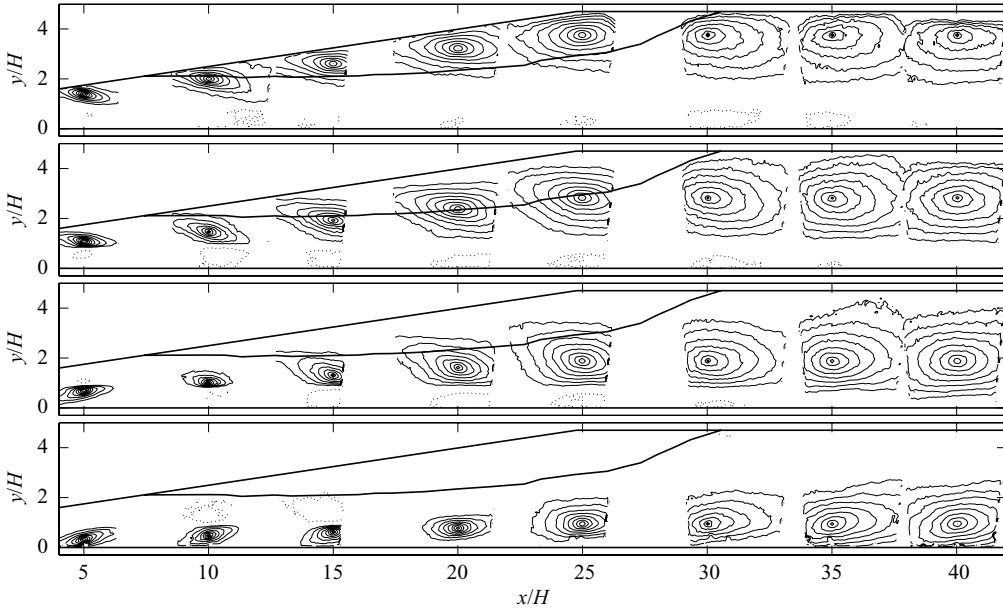
FIGURE 26. Correlation coefficients R_{uu} at $x/H = 5, 10, 15, 20, 25, 30, 35, 40$ and $y/h(x) = 0.2$, 0.4, 0.6, 0.8. The solid contours show R_{uu} between 0.2 and 1 with an increment of 0.1 and the dotted contours represent $R_{uu} = -0.1$. The thick black contour shows the mean streamline enclosing the recirculation region.
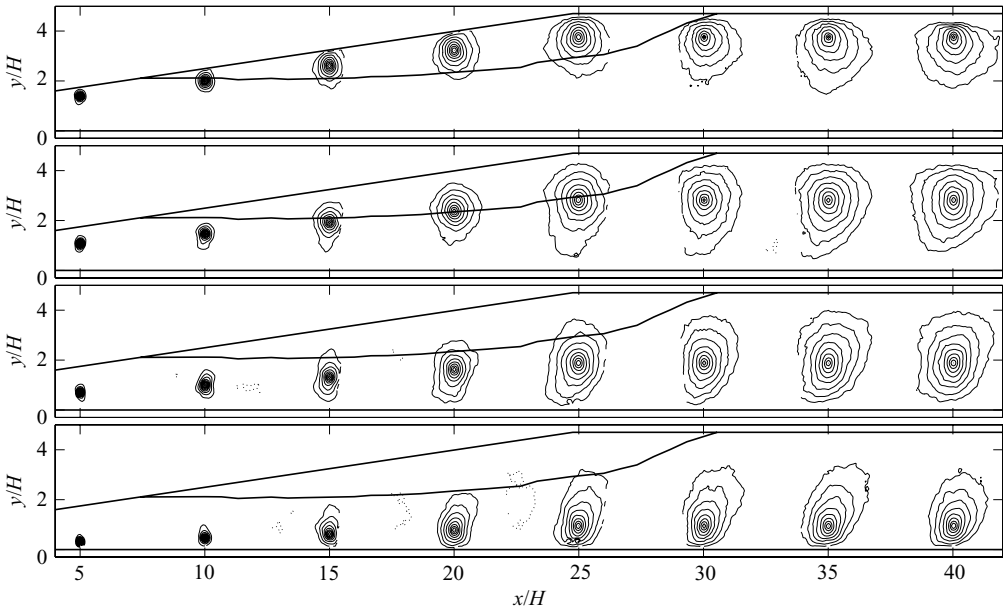

FIGURE 27. Correlation coefficients R_{vv}. Positions and contour levels
are the same as in figure 26.

correlations suggests that large-scale vortices with their axes aligned with the major axes of the R_{ww} correlation peaks are common in this flow. Studies of structures of the spanwise velocity fluctuations in an xy plane are surprisingly few and we have
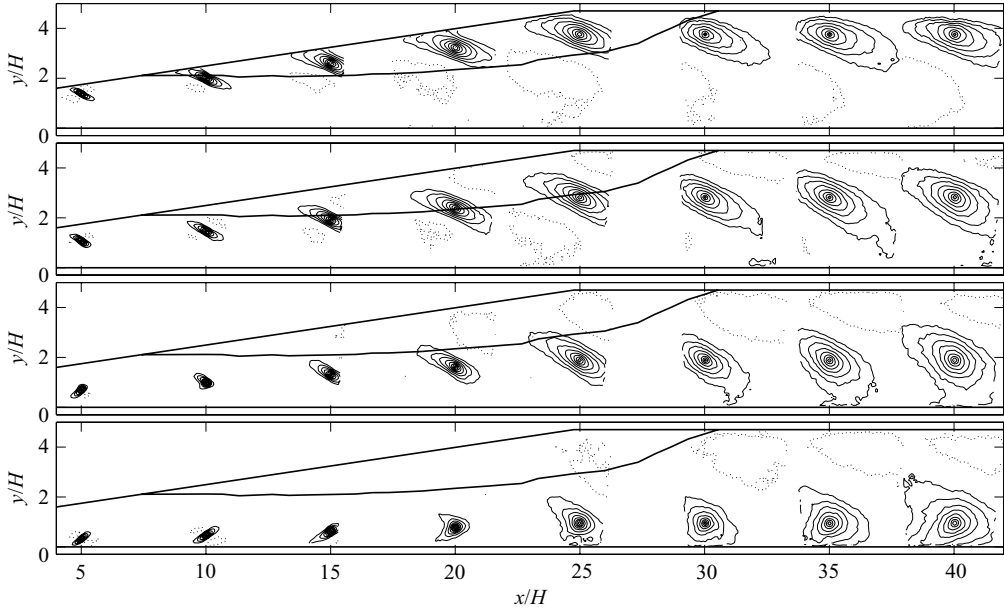
FIGURE 28. Correlation coefficients R_{ww}. Positions and contour levels are the same
as in figure 26.

not been able to find any investigation discussing these structures and particularly
not in conjunction with hairpin or horseshoe vortices.

5. Summary and conclusions

The flow in an asymmetric plane diffuser has been studied with extra attention
paid to ensuring good two-dimensionality of the mean flow and minimizing the
measurement errors. The Reynolds number based on the inlet bulk flow velocity, U_b,
and the inlet channel height, H, was approximately 38 000.

The profiles of the streamwise mean velocity, U, reveal a flow divided into a
high-velocity region following the plane wall and a low velocity region with flow
reversal near the inclined wall. In between these regions there is a strong shear
layer. The differences between the regions diminish gradually in the exit channel after
reattachment.

The velocity in the y-direction, V, is very small in most parts of the diffuser, but
close to the upstream corner at the diffuser inlet where the change in the direction
of the wall is rather abrupt, locally high values of V and strong streamline curvature
are found. The mean flow separates on the inclined wall at 7.4 inlet channel heights
downstream the diffuser inlet. Instantaneous flow reversal occurs upstream the mean
separation point but never above $x/H = 5$ as shown by the backflow coefficient.
Instantaneous flow reversal occurs far downstream the mean reattachment point
which was found to be at $x/H = 30.5$. The backflow coefficient shows that nowhere
in the diffuser is the flow reversed more than 90 % of the time.

High turbulence levels were found in the strong shear layer forming between the
separation bubble and the high-velocity region. The normal Reynolds stresses have
similar profiles, with broad global maxima between $x/H = 20–25$. The streamwise
turbulence component has the largest magnitude, about twice that of the other two

normal components. The production rate of turbulent kinetic energy is shown to peak farther upstream as compared to the Reynolds stresses. Negative values of the production rate indicate that the mean flow gains energy from the turbulence close to the wall in the downstream end of the reversed flow region. This is an aspect that will be investigated in more detail in a separate study.

The relation between the momentum loss in the diffuser and the pressure forces was investigated and it was found that most of the momentum losses are due to the pressure forces and that only a small part of the momentum loss is caused by skin friction on the walls. An investigation of terms in the mean kinetic energy equation shows that production of turbulence is the main consumer of mean flow mechanical energy in the diffuser.

Energy spectra, instantaneous velocity fields and spatial auto-correlations indicate that the turbulence is partly broken down to smaller scales in the separated region near reattachment.

The existence of large-scale hairpin- or horseshoe-like structures in this flow is supported by (*i*) the shape of the auto-correlation functions of the spanwise velocity; (*ii*) the frequently observed pairs of, one positive and one negative, elongated and inclined structures of spanwise velocity; and (*iii*) the sequence of vector fields showing the disappearance of a pair of the previously described structures, due to large-scale spanwise fluctuations, and the subsequent appearance of an ejection event.

We have found no previous investigation where the structure of the spanwise velocity fluctuations in an xy plane is discussed. The inclined structures observed can, for example, be seen in figure 21 of Le, Moin & Kim (1997), showing an instantaneous field, but the structures are not commented in the article.

The formation of large-scale regions of backflow near the separation point appears to be a result of large-scale fluctuations of undulating character that cannot be related to any distinct vortices. However, farther downstream it is observed that ejection events related to hairpin structures could give rise to local regions of flow reversal.

The 8.5° plane asymmetric diffuser flow-case has been shown to exhibit several interesting phenomena that challenge the turbulence models of today, such as plane wall separation and reattachment, strong and sudden shearing, non-equilibrium turbulence and turbulence relaxation.

REFERENCES

ADRIAN, R. J., CHRISTENSEN, K. T. & LIU, Z.-C. 2000*a* Analysis and interpretation of instantaneous turbulent velocity fields. *Exp. Fluids* **29**, 275–290.

ADRIAN, R. J., MEINHART, C. D. & TOMKINS, C. D. 2000*b* Vortex organization in the outer region of the turbulent boundary layer. *J. Fluid Mech.* **422**, 1–54.

BRÜGER, A., NILSSON, J., KRESS, W., STÅLBERG, E., GUSTAFSSON, B., LÖTSTEDT, P., JOHANSSON, A. V. & HENNINGSON, D. S. 2004 A hybrid high order method for incompressible flow in complex geometries. *Tech. Rep.* TRITA-MEK 2004:11. KTH Mechanics.

BUICE, C. U. & EATON, J. K. 1997 Experimental investigation of flow through an asymmetric plane diffuser. *Tech. Rep.* Department of Mechanical Engineering, Stanford university.

BUICE, C. U. & EATON, J. K. 2000 Experimental investigation of flow through an asymmetric plane diffuser. *J. Fluids Engng* **122**, 433–435.

COMTE-BELLOT, G. 1965 Écoulement turbulent entre deux paroix parallèles. Publications scientifiques et techniques 419. Ministère de l'air, 2, Avenue de la Porte-d'Issy, Paris.

VAN DOORNE, C. W. H. 2004 Stereoscopic PIV on transition in pipe flow. PhD thesis, Technische Universiteit Delft.

FOUCAUT, J., CARLIER, J. & STANISLAS, M. 2004 PIV optimization for the study of turbulent flow using spectral analysis. *Meas. Sci. Technol.* **15**, 1046–1058.

GULLMAN-STRAND, J. 2004 Turbulence and scalar flux modelling applied to separated flows. PhD thesis, KTH Mechanics, Stockholm, Sweden.

GULLMAN-STRAND, J., TÖRNBLOM, O., LINDGREN, B., AMBERG, G. & JOHANSSON, A. V. 2004 Numerical and experimental study of separated flow in a plane asymmetric diffuser. *Intl J. Heat Fluid Flow* **25**, 451–460.

HELLSTEN, A. & RAUTAHEIMO, P. (Ed.) 1999 *Workshop on Refined Turbulence Modelling*. ERCOFTAC/IAHR/COST.

HERBST, A. H. 2006 Numerical studies of turbulent and separated flows. PhD thesis, KTH Mechanics, Stockholm, Sweden.

JOHANSSON, A. V. & ALFREDSSON, P. H. 1981 Development of a water tunnel for studies of turbulent shear flows. *Tech. Rep.* TRITA-MEK-81-01. Royal Institute of Technology.

KALTENBACH, H.-J., FATICA, M., MITTAL, R., LUND, T. S. & MOIN, P. 1999 Study of flow in a planar asymmetric diffuser using large-eddy simulation. *J. Fluid Mech.* **390**, 151–185.

KEANE, R. & ADRIAN, R. 1992 Theory of cross-correlation in PIV. *Appl. Sci. Res.* **49**, 191–215.

KEANE, R. D. & ADRIAN, R. J. 1990 Optimization of particle image velocimeters. Part I. double pulsed systems. *Meas. Sci. Technol.* **1**, 1202–1215.

KROGSTAD, P.-Å. & ANTONIA, R. A. 1994 Structure of turbulent boundary layers on smooth and rough walls. *J. Fluid Mech.* **277**, 1–21.

LE, H., MOIN, P. & KIM, J. 1997 Direct numerical simulation of turbulent flow over a backward-facing step. *J. Fluid Mech.* **330**, 349–374.

OBI, S., AOKI, K. & MASUDA, S. 1993a Experimental and computational study of turbulent separating flow in an asymmetric plane diffuser. In *Ninth Symp. on Turbulent Shear Flows*, Kyoto, Japan.

OBI, S., ISHIBASHI, N. & MASUDA, S. 1997 The mechanism of momentum transfer enhancement in periodically perturbed turbulent separated flow. In *Second Intl Symp. on Turbulence, Heat and Mass Transfer*, pp. 835–844. Delft, The Netherlands.

OBI, S., NIKAIDO, H. & MASUDA, S. 1999 Reynold number effect on the turbulent separating flow in an asymmetric plane diffuser. In *Proc. FEDSM99*, *FEDSM* 99-6976 (ASME/JSME Fluids Engineering Division Summer Meeting).

OBI, S., OHIZUMI, K., AOKI, K. & MASUDA, S. 1993b Turbulent separation control in a plane asymmetric diffuser by periodic perturbation. In *Engineering Turbulence Modelling and Experiments 2*, pp. 633–642. Elsevier.

RAFFEL, M., WILLERT, C. & KOMPENHANS, J. 1997 *Particle Image Velocimetry, A Practical Guide*. Springer.

SCARANO, F. & RIETHMULLER, M. L. 2000 Advances in iterative multigrid PIV image processing. *Exp. Fluids* **29** (Suppl.), S51–S60.

SIMPSON, R. L. 1989 Turbulent boundary-layer separation. *Ann. Rev. Fluid Mech.* **21**, 205–234.

SONG, S. & EATON, J. K. 2004 Flow structures of a separating, reattaching and recovering boundary layer for a large range of Reynolds number. *Exp. Fluids* **36**, 642–653.

TÖRNBLOM, O. 2006 Experimental and computational studies of turbulent separating internal flows. PhD thesis, KTH Mechanics, Stockholm, Sweden.

WESTERWEEL, J. 1997 Fundamentals of digital particle image velocimetry. *Meas. Sci. Technol.* **8**, 1379–1392.

WIENEKE, B. 2005 Stereo-PIV using self-calibration on particle images. *Exp. Fluids* **39**, 267–280.

WU, X., SCHLÜTER, J., MOIN, P., PITSCH, H., IACCARINO, G. & HAM, F. 2006 Computational study on the internal layer in a diffuser. *J. Fluid Mech.* **550**, 391–412.